Beyond A and B Compartments: how major nuclear locales define nuclear genome organization and function

Omid Gholamalamdari[#1], Tom van Schaik[#2], Yuchuan Wang[#3], Pradeep Kumar[#1], Liguo Zhang[#1], Yang Zhang[#3], Gabriela A. Hernandez Gonzalez[1], Athanasios E. Vouzas[4], Peiyao A. Zhao[4], David M. Gilbert[*4], Jian Ma[*3], Bas van Steensel[*2], Andrew S. Belmont[*1,6,7]

[#] These authors contributed equally to this work

[1]*Department of Cell and Developmental Biology, University of Illinois at Urbana-Champaign, Urbana, IL 61801, USA*

[2]*Division of Gene Regulation and Oncode Institute, Netherlands Cancer Institute, Amsterdam 1066, Netherlands*

[3]*Ray and Stephanie Lane Computational Biology Department, School of Computer Science, Carnegie Mellon University, Pittsburgh, PA 15213, USA*

[4]*San Diego Biomedical Research Institute, San Diego, CA, 92121, USA*

[6]*Center for Biophysics and Quantitative Biology, University of Illinois at Urbana-Champaign, Urbana, IL 61801, USA*

[7]*Carl R. Woese Institute for Genomic Biology, University of Illinois at Urbana-Champaign, Urbana, IL 61801, USA*

Abstract:

Models of nuclear genome organization often propose a binary division into active versus inactive compartments, yet they overlook nuclear bodies. Here we integrated analysis of sequencing and image-based data to compare genome organization in four human cell types relative to three different nuclear locales: the nuclear lamina, nuclear speckles, and nucleoli. Whereas gene expression correlates mostly with nuclear speckle proximity, DNA replication timing correlates with proximity to multiple nuclear locales. Speckle attachment regions emerge as DNA replication initiation zones whose replication timing and gene composition vary with their attachment frequency. Most facultative LADs retain a partially repressed state as iLADs, despite their positioning in the nuclear interior. Knock out of two lamina proteins, Lamin A and LBR, causes a shift of H3K9me3-enriched LADs from lamina to nucleolus, and a reciprocal relocation of H3K27me3-enriched partially repressed iLADs from nucleolus to lamina. Thus, these partially repressed iLADs appear to compete with LADs for nuclear lamina attachment with consequences for replication timing. The nuclear organization in adherent cells is polarized with nuclear bodies and genomic regions segregating both radially and relative to the equatorial plane. Together, our results underscore the importance of considering genome organization relative to nuclear locales for a more complete understanding of the spatial and functional organization of the human genome.

Introduction:

Over 100 years of cytology has recognized characteristic features of nuclear genome organization, including blocks of condensed chromatin enriched at the nuclear and nucleolar peripheries and varying degrees of condensation/decondensation throughout the nuclear interior. Foci of active transcription are concentrated at the edges of chromosome territories and sub-territory condensed chromatin masses and depleted at the nuclear periphery (Belmont, 2022; Bernhard and Granboulan, 1963; Cremer et al., 2015; Cremer and Cremer, 2006; Misteli, 2020; Politz et al., 2013, 2016; Takizawa et al., 2008; van Steensel and Belmont, 2017). Two current models for nuclear genome organization prevail (Belmont, 2022). The radial genome organization model describes a radial gradient of higher gene expression activity towards the nuclear center (Bickmore, 2013; Croft et al., 1999; Girelli et al., 2020; Kolbl et al., 2012; Kupper et al., 2007; Takizawa et al., 2008). The binary model of genome organization describes the differential intranuclear positioning of a peripheral, lamina-associated, late-replicating, transcriptionally inactive Hi-C B compartment versus an interior, early-replicating, transcriptionally active Hi-C A compartment (Guelen et al., 2008; Kind et al., 2013; Lieberman-Aiden et al., 2009; Peric-Hupkes et al., 2010; Ryba et al., 2010; White et al., 2004)

However, neither model acknowledges the considerable cell-type specific variability in nuclear shape and size, as well as the size, number, and relative positioning of nuclear bodies. This variability could dramatically affect chromosome trajectories and the distribution of active and inactive chromatin regions among nuclear locales. Indeed, high-resolution Hi-C has identified two active A subcompartments and three major repressive B subcompartments (Rao et al., 2014). Similarly, TSA-seq, NAD-seq, and SPRITE have distinguished between types of

heterochromatin localizing preferentially at nucleoli versus the nuclear lamina and have revealed a type of active chromatin specifically localizing near nuclear speckles (Chen et al., 2018; Nemeth et al., 2010; Quinodoz et al., 2021, 2018; van Koningsbruggen et al., 2010; Vertii et al., 2019; Zhang et al., 2020). However, most previous studies have not attempted to combine multiple genomic readouts across multiple cell types.

Here we integrate light microscopy imaging of major nuclear locales- the nuclear lamina, nucleoli, and nuclear speckles- with DamID (Guelen et al., 2008; van Schaik et al., 2020), TSA-seq (Zhang et al., 2020), and high-resolution Repli-seq (Zhao et al., 2020) genome mapping to investigate how the genome is both spatially and functionally organized relative to nuclear locales across four human cell types hTERT-immortalized human foreskin fibroblasts (HFFc6, abbreviated hereafter as HFF), H1 human embryonic stem cells (hESCs), HCT116 (HCT) colon carcinoma epithelial cells, and K562 erythroleukemia cells.

RESULTS

Cell types differ widely in morphology and arrangement of nuclear locales

Prior analyses have largely overlooked the possible contribution of nuclear and nuclear body morphology to nuclear genome positioning. To measure sizes and shapes of nuclei and nuclear bodies, cell lines were stained for nuclear speckles (hereafter referred to simply as speckles), nucleoli, and the nuclear periphery (NP) with anti-SON, anti-MKI67IP, and anti-glycosylated nucleoporin (anti-RL1) antibodies, respectively, and for DNA using DAPI. Deconvolved wide-field microscopy images (**Fig. 1A**) were then segmented to generate nuclear 3D models (**Fig. 1B, SFig. 1A**).

K562 and H1 nuclei have larger volume (V), lower surface area (SA), and are rounder (lower SA/V) as compared to HCT and HFF nuclei (**Fig. 1C**). Whereas K562 and H1 speckles distribute radially in 3D, surrounding nucleoli and concentrating within the nuclear interior, HCT and HFF speckles preferentially distribute in the equatorial (center) z-planes while being depleted radially near the nuclear periphery within these equatorial planes (**Fig. 1B**). H1 and HCT116 have large, often single, nuclear-centrally located nucleoli, while HFF and K562 have smaller, multiple nucleoli distributed between speckles (**Fig. 1A, B, D**). Total nucleolar volumes per nucleus are largest in HCT116 and lowest in HFF (**Fig. 1D**).

We compared relative arrangements of these nuclear locales across cell lines by measuring the nearest distances between these locales (**SFig. 1B**). Rounder nuclei (K562, H1) have significantly larger speckle-to-NP and nucleolus-to-NP distances compared to flatter nuclei (HFF, HCT116) as expected (**SFig. 1C**, **Fig. 1E**). But speckle-to-nucleoli distances in K562 are lower than other cell lines, with HFF showing noticeably larger speckle-to-nucleoli distances

(**SFig. 1C**, **Fig. 1E**). While total speckle and nucleolar volumes scale linearly with nuclear volume in all cell lines, curiously total speckle volume correlates more strongly with nuclear surface area versus volume (**SFig. 1D**).

Overall, the four cell lines divide approximately into round (K562, H1) nuclei with radial organization of nuclear bodies versus flat nuclei (HCT116, HFF) with nuclear bodies distributed relative to both x-y radial and z-axes. This division is further supported by Principal Component Analysis (PCA) using 14 morphological measures (**Fig. 1F, SFig. 1F**).

Global differences in nuclear genome organization in different cell types revealed by DamID and TSA-seq

We next surveyed genome organization relative to the NP, using nuclear lamina (lamina) as a target, speckles, and nucleoli by applying LMNB1 (lamina) DamID and LMNB1 (lamina), SON (speckle), and MKI67IP (nucleolus) TSA-seq (**Fig. 2A**). Speckle TSA-seq is highly conserved across all four cell types (**Fig. 2A**), as described previously (Zhang et al., 2020) and supported here by the high correlations for speckle TSA-seq comparisons between pairs of cell lines, despite a lower dynamic range in HCT116 and especially HFF (**Fig. 2B**). In contrast, genome-wide correlations in pair-wise cell line comparisons were substantially lower for lamina DamID and for both lamina and nucleolus TSA-seq as compared to speckle TSA-seq (**Fig. 2A-B, SFig. 2A-C**). For example, LADs near the ends of long chromosome arms switch from a strong lamina association in HFF and HCT116 to a more interior and nucleolar association in H1 and K562 (Fig. S2A). While in HCT116 cells local maxima in nucleolar TSA-seq align with LADs, in HFF, H1, and

K562 cells small peak and “peak-within-valley” nucleolar TSA-seq local maxima instead align with speckle TSA-seq peaks (**Fig. S2B**).

These results suggest that genome positioning relative to speckles is highly conserved across cell lines, despite variations in speckle intranuclear positioning (**Fig. 1**). In contrast, major variations exist across different cell types for genome positioning relative to the lamina and nucleoli.

Gene expression and DNA replication timing exhibit distinct correlations with nuclear locales

We previously identified genomic regions 100 kb or larger, comprising ~10% of the genome, that showed statistically significant differences in speckle TSA-seq smoothed scores in pairwise comparisons between the same four cell lines (Zhang et al., 2020). Genes within these regions showed a strong positive correlation between differences in their gene expression and speckle positioning. Chromosome regions with different position relative to speckles typically show inverse differences in their position relative to the lamina (**SFig. 2D**, top panels), though individual genome regions have variable magnitude and even direction of these differences (SFig. 2E). However, the reverse is not true. Pairwise cell-line comparisons reveal ~40-70% of the genome shows statistically significant differences in lamina TSA-seq over regions 100 kb or larger, with most of these regions showing little or no differences in speckle TSA-seq scores (**SFig. 2D-E**, bottom panels).

Genes within genomic regions displaying significant differences in speckle TSA-seq in cell line comparisons tend to show increased expression when they are closer to speckles and decreased expression when they are further from speckles (**Fig. 2C**), as described previously

(Zhang et al., 2020). In contrast, genes within genomic regions which in pair-wise comparisons of cell lines show a statistically significant difference in lamina TSA-seq show no obvious trend in their expression differences (**Fig. 2C**).

Binning all genes as a function of differences in their normalized speckle, nucleolar, and lamina TSA-seq scores show a positive correlation of differences in gene expression with changes in speckle TSA-seq scores but no apparent correlation with differences in lamina or nucleolar TSA-seq scores (**Fig. 2D**). Linear modeling for correlation between changes in gene expression and changes in TSA-seq reveals a substantially stronger correlation for positioning relative to speckles, as compared to positioning relative to the lamina or nucleoli (**Fig. 2E, SFig. 2F**); this pattern holds genome-wide (**Fig.2E**) as well as for correlations over specific genome region types (LAD, iLAD, speckle TSA-seq maxima) (**SFig. 2F**). Instead, pair-wise cell type comparisons revealed significant correlations between changes in DNA replication timing and changes in TSA-seq with respect to all three locales- speckle, lamina, and nucleoli (**Fig. 2F-G**).

In summary, whereas gene expression primarily correlates with relative distance to nuclear speckles, DNA replication timing correlates with relative distance to all three nuclear locales, despite the variable positioning of nuclear speckles and nucleoli across cell types.

Both Type I and Type II speckle attachment regions are gene expression hot-zones and DNA replication IZs but show varying gene composition and DNA replication timing

We next sought to determine the relationship between gene expression "hot-zones" (Chen et al., 2018) embedded within larger iLAD/A compartment regions and speckle association. We first identified larger amplitude (Type I) SON TSA-seq local maxima embedded

within A1 Hi-C subcompartments versus smaller amplitude (Type II) local maxima embedded within A2 Hi-C subcompartments (red versus blue tick marks, **Fig. 3A**).

Type I peaks showed a near unimodal distribution of distance to the nearest speckle with a peak at ~100 nm distance (**Fig. 3B**), based on IMR90 fibroblast multiplexed FISH data (Su et al., 2020), used as a proxy for HFF fibroblast measurements. In contrast, Type-II peaks showed a bimodal speckle distance distribution (Hartigan's dip test (Hartigan and Hartigan, 1985), p-value < 0.05, (**SFig. 3A**)), with one narrow peak similarly located at ~100 nm distance and a broader peak centered at ~500 nm from speckles (**Fig. 3B**). Notably, Type II peaks show a lower speckle association frequency (<250 nm threshold, **Fig. 3B**, dashed line) than Type I peaks (**Fig. 3C**), suggesting that while Type II peaks still associate specifically with speckles their interaction with speckles is weaker and/or less frequent as compared to Type 1 peaks.

Both Type I (red) and Type II (blue) average peak widths are ~400kb (**Fig. 3D**)**;** however, Type I peaks have higher speckle TSA-seq and Hi-C compartment scores (**Fig. 3D**) and contain shorter genes, genes with smaller exon and intron length, and genes with lower fractional intron composition (**SFig. 3B**). Across the four cell types, Type I peaks also are more conserved than Type II peak (Jaccard indexes of 0.85 versus 0.67 for Type 1 versus Type 2) (**SFig. 3C**).

Although gene expression levels are similar over Type I and II peaks (**Fig. 3D**, 2nd from right), the IMR90 multiplexed image data reveals a trend of gene loci within Type I peaks showing a higher fraction of "ON" states among the cell population as compared with gene loci within Type II peaks (**SFig. 3D**).

Both Type I and Type II peaks align with DNA replication initiation zones (IZs), identified as peaks in 16-fraction Repli-seq (**Fig. 3A**). Type I peaks replicate slightly earlier than Type II

peaks (**Fig. 3E-F**, **SFig. 3E**), although this difference is noticeably larger in HCT116 versus H1 cells (**Fig. 3A,E,F**). Speckle TSA-seq scores progressively decrease with later replication timing of IZs (**Fig.3F**). However, DNA replication timing variability (Twidth) is notably larger for Type II peaks, particularly in HCT116 (**Fig. 3E**, **SFig. 3E**) suggesting a possible link between variability in speckle association (**Fig. 3B**) and variability in DNA replication timing (Fig. 3E).

We next used live-cell imaging to corroborate that chromosome regions close to nuclear speckles, primarily Type I peaks, would show the earliest DNA replication timing. Indeed, in HCT116 cells expressing EGFP-SON and mCherry-PCNA, the first PCNA foci appearing within the first 30 mins of S-phase were nearly 100% localized within 500 nm of speckles (**SFig. 3F**). From 30 to 135 mins after initiation of S-phase, more PCNA foci appeared at increasing distances from speckles (**SFig. 3F**).

These results show that while Type I and II speckle-associated regions are both DNA replication IZs and show similarly elevated levels of gene expression, they contain different types of genes, show different speckle association frequencies, and show different timing of DNA initiation.

LAD to iLAD conversions mostly correspond to transitions from a repressed/ late-replicating to an intermediate repressed/ late-to-middle DNA replicating chromatin state

The low correlation between differences in gene expression with differences in lamina and/or nucleolar TSA-seq and lamina DamID scores (**Fig. 2D&E**, **SFig. 2D&E**) suggested that transitions from facultative LAD (fLAD) to facultative iLAD (fiLAD) might not strictly represent a binary transition from repressed to active chromatin. Analysis across cell lines reveals that

lamina DamID scores of a fLAD genomic region can continuously transition from positive peaks in lamina DamID (red rectangles), to peak-within-valley (p-w-v) local maxima (yellow rectangles), or to valleys (v) (blue rectangles) (**Fig. 4A, SFig. 4A**). A subset of p-w-v fiLADs also showed p-w-v local maxima in their lamina TSA-seq signals together with p-w-v local maxima or small positive peaks in their nucleolus TSA-seq signals (**SFig. 4A**).

We implemented an algorithm to define these three domain classes genome-wide based on their local relative increase ("enrichment") in DamID score (**SFig. 4B**) (See Methods), revealing that p-w-v fiLADs are more common than v-fiLADs in all cell lines except HFF, which has few fiLADs of either type (**Fig. 4B-C**). The transitions between LADs, p-w-v fiLADs and v-fiLADs are highly dynamic across the four cell lines (**Fig. 4A, SFig. 4C)**, with some regions transitioning between all three domain types among the four cell lines (**Fig. 4A, SFig. 4A & C**). We observe an increasing number (**Fig. 4B**) and total genome coverage (**Fig. 4C**) of LADs versus p-w-v fiLADs and v-fiLADs comparing H1, K562, HCT116, and HFF cell lines.

p-w-v fiLADs show late to middle DNA replication timing and reduced gene expression levels, rather than the early DNA replication timing and higher gene expression typical of constitutive iLADs (ciLADs) and a subset of v-fiLADs (**Fig. 4A-B, SFig. 4D**). Moreover, transitions between cell lines from p-w-v- to v-fiLADs show an increase in gene expression of comparable magnitude to that observed in LAD to p-w-v fiLAD transitions (**Fig. 4D**, **SFig. 4E**). While p-w-v fiLADs are classified as A compartment, with positive Hi-C compartment scores, in pile-up plots they show lower compartment scores than iLAD or v-fiLAD regions (**Fig. 4E**). Both p-w-v-fiLADs and v-fiLADs have earlier replication timing than LADs, but p-w-v fiLADs replicate later than v-fiLADs (**Fig. 4E-F**). Additionally, p-w-v fiLADs typically have an intermediate chromatin state

between LADs and v-fiLADs, as defined by their relatively increased levels of “repressive” and decreased levels of “active” histone marks (**SFig. 4F**).

In summary, p-w-v fiLADs, comprising the majority of fiLADs, retain some heterochromatic marks and repressive functional properties as compared to v-fiLADs, which instead show an earlier-replicating, more active chromatin state comparable to typical iLADs.

p-w-v fiLADs compete with LADs for nuclear lamina association; linking nuclear lamina association with later DNA replication timing but not lower gene expression

To probe the functional consequences of nuclear lamina genome association, we made LMNA, LBR, and double LMNA/LBR K562 knockout (KO) lines. Whereas the LMNA KO shows little change in lamina DamID from K562 wild-type (wt) or the parental clone, the LBR KO and the LMNA/LBR double knockout (DKO) lines show similar but partial reduction in the lamina DamID for most LADs and increases for some iLADs (**SFig. 5A**). Therefore, we focused our attention on comparisons between wt K562 and the DKO line.

DKO cells showed loss of the nuclear lobulation characteristic of wtK562 nuclei, the appearance of a DAPI-dense perinucleolar rim not apparent in the wtK562 nuclei, and an increased number of DAPI-dense foci in the nuclear interior (**Fig. 5A**). Based on DamID and TSA-seq, most LADs in DKO cells decrease their interaction and relative proximity with the lamina and increase their proximity to nucleoli but maintain their positioning to speckles (**Fig. 5B, SFig. 5B**). Unexpectedly, most p-w-v-fiLADs instead increase their lamina association while decreasing their proximity to nucleoli (**Fig. 5B**, **SFig. 5B-C**). Indeed, most of these p-w-v fiLADs

become actual LADs in the DKO (**SFig. 5D**); some v-fiLADs also become LADs in the DKO (which may be due to a misclassification of v- versus p-w-v fiLADs) (**SFig. 5C-D**).

Scatterplots comparing changes in lamina and nucleolar TSA-seq scores between wt and DKO showed an inverse relationship (**Fig. 5C**). This shift correlates with ChIP-seq data, showing that regions enriched in H3K27me3 generally shift away from nucleoli towards the lamina in the DKO, while the opposite trend is observed for regions enriched in H3K9me3 (**Fig. 5D**) (consistent with the enrichment of H3K27me3 in p-w-v fiLADs versus H3K9me3 in LADs (**SFig. 4F**)).

Despite the wide-spread genomic shifts relative to the lamina and nucleolus, only a small number of genes significantly change their gene expression in the KO and DKO lines (**Fig. 5F**). Moreover, there is no obvious bias in the direction of gene expression changes as a function of changes in the lamina DamID between the DKO and wt (**Fig. 5G**). Similarly, there is no obvious bias towards increased gene expression among those genes contained specifically within wt LADs that change their expression and also show reduced lamina interaction (decreased lamina DamID) in the DKO **(SFig. 5E**). (However, there is an intriguing bias of an increased fraction of differentially expressed genes in LADs versus iLADs in all KO cell lines (**SFig 5F-G**)).

In contrast, plotting 2-fraction Repli-seq versus changes in DamID shows a consistent trend of slightly later DNA replication timing for regions (primarily p-w-v fiLADs) moving closer to the lamina (**Fig. 5B&G**). However, LADs that shift further away from the lamina, do not show an obvious progressive shift towards earlier DNA replication timing (**Fig. 5B&G, SFig. 5H**).

Differential positioning relative to speckles and lamina identifies different types of LAD regions

We next used differences in lamina versus speckle TSA-seq scores to identify heterochromatin regions with differential biochemical and functional properties (**Fig. 6**, **SFig. 6**).

First, whereas an overall inverse relationship between lamina and speckle TSA-seq observed in K562 cells is largely preserved in H1 cells, scatterplots reveal off-diagonal genomic bins ("H1 ROI" orange bins in **Fig. 6A**, "H1 ROI C1&C2" in **SFig. 6A**) with disproportionally low lamina TSA-seq scores (**Fig. 6A&B**, **SFig A&B**). These genomic bins are largely within several Mbp from centromeres (**Fig. 6C, SFig. 6E**), are H3K9me3-enriched (**Fig. 6D**), and are more associated with the nucleolus specifically in H1 cells in which they are less associated with the lamina (**SFig. 6B-C**). Many genomic regions contained within the H1 ROI-C1 display a similar position in the K562 DKO scatterplot (**SFig. 6D**), suggesting a LMNA and/or LBR dependence for nuclear lamina association for this subgroup of LADs.

Second, deviations in the inverse relationship between SON and lamin TSA-seq in HCT116 and HFF cells with flat nuclei reveals four types of LAD regions, defined by DamID (**SFig. 6F**), varying in their histone modifications **(Fig. 6E-F**): 1) H3K9me3-enriched LAD Cluster C1: low SON, high LMNB1; 2) H3K27me3-enriched LAD Cluster C2: moderate SON, high LMNB12; 3) H3K9me2- and H2A.Z-enriched LAD Cluster C3: low SON, low LMNB1; 4) low in multiple histone marks LAD Cluster C4: moderate SON, low LMNB1. Superimposing these histone mark enrichments over the HCT116 scatterplot more precisely revealed the differential spatial distribution of LAD regions with different types of histone mark enrichments (**Fig. 6G**).

These four types of LAD regions show different correlations with both gene expression levels and DNA replication timing (**Fig. 6H**). H3K9me3-enriched C1 LAD regions show the lowest levels of gene expression. H3K27me3-enriched C2, H3K9m2/H2A.Z-enriched C3, and C4 LAD regions show gene expression levels significantly lower than iLADs but slightly higher than C1 LAD regions. DNA replication timing is latest and most uniform for the C1 LAD regions and shows progressively earlier DNA replication timing for the C3, C2, and C4 LAD regions which all still replicate later than iLADs. We defined a “constitutive LAD (cLAD) score" as the number of cell lines out of 7 overall in which a chromosome region is a LAD. cLADs are enriched over LAD regions with the lowest SON TSA-seq scores (C1 and C3) while fLADs are enriched over LAD regions with moderate SON TSA-seq scores (C2 and C4) (**Fig 6J**).

In summary, LAD regions that segregate differentially relative to speckles and the lamina show different histone mark-enrichments and functional properties.

Polarity of Nuclear Genome Organization

The loss of the strong inverse relationship between speckle and lamina TSA-seq in the HCT116 and HFF cell lines was unexpected and puzzling. The noticeably weaker inverse relationship between speckle and lamina TSA-seq in cells with flat (HCT116, HFF) versus round nuclei (K562, H1) was due specifically to changes in lamina TSA-seq as lamina DamID scores showed less variation across cell lines.

We hypothesized that LADs lying within the nuclear equatorial plane in flat nuclei would have the highest lamina TSA-seq scores: after lamina TSA-staining they would be exposed to a higher concentration of tryamide free-radicals generated and diffusing from the nearby side,

top, and bottom of the nuclear lamina as compared to LADs at either the top or bottom of the nuclear lamina. We simulated this effect by convolving the HFF anti-RL1 immunostaining image with a kernel corresponding to the exponential diffusion gradient of tyramide-biotin TSA labeling, yielding a notably elevated TSA signal in the equatorial plane of the nuclear periphery (**Fig. 7A**).

Using the IMR90 multiplexed FISH data set [43], we compared the localization in HFF cells of 26 LADs mapping to regions of highest lamina TSA-seq (Cluster 1, **Fig. 7B**) versus 27 LADs mapping to regions of lowest speckle TSA-seq but with low to moderate lamina TSA-seq (Cluster 2, **Fig. 7B**). Cluster 1 LADs showed a biased localization in IMR90 fibroblasts towards the equatorial plane as compared to Cluster 2 LADs that distributed more uniformly over the x-y nuclear projection (**Fig. 7C**). More generally, Cluster 1 and 2 LADs show a similar differential localization in lamina versus SON TSA-seq scatterplots in HFF and HCT116 cells with flat nuclei which is notably different than in K562 and H1 cells with round nuclei (**SFig. 7A**). Cluster 1 LADs correspond to LADs located towards the ends of long chromosome arms (**SFig. 7B).** Overall, in fibroblasts there is a trend of distal chromosome arms localizing preferentially towards the nuclear equator versus centromeric regions localizing preferentially towards the nuclear center (**Fig. 7D-E and SFig. 7C-D**).

We next examined the nuclear polarity of genomic regions associated with different nuclear locales in fibroblasts. Single cell data (**SFig. 7E**) and average trends over all nuclei (**SFig. 7F**), show speckle-associated regions concentrated towards the equatorial plane, consistent with the direct localization of speckles within the equatorial plane (**Fig. 1B**). Nucleolus-associated regions were distributed towards the nuclear center but throughout the z-plane

(**SFig. 7E-F**). Type I speckle attachment regions localize more centrally in the x-y plane and closer to the equatorial plane than Type II speckle attachment regions (**Fig. 7F-G, SFig. 7G**). The closer lamina proximity for Type II peaks is consistent with the shorter genomic distances of Type II versus I peaks to the nearest LADs ([1] and data not shown). fLADs localize to equatorial plane (Fig. 7G) consistent with the enrichment of H3K27me3 modification in these regions, while cLADs localize furthest away from this plane (Fig. 7G). Additionally, v-fiLADs cluster closer to the equatorial plane and further from the nuclear center as compared to p-w-v fiLADs (**SFig. 7I**).

To more comprehensively survey how the genome distributes relative to nuclear polarity, we turned to the use of SPIN states, which combine TSA-seq and DamID with Hi-C data to segment the genome into 9-10 states based on their intranuclear localization; SPIN states show differential epigenetic marks, gene expression, and DNA replication timing (Wang, 2021; Wang et al., 2021). SPIN states ordered according to highest to lowest gene expression, and earliest to latest DNA replication timing, showed a pronounced, nearly monotonic increasing distance from the equatorial plane (**Fig. 7G**) as well as differential localization relative to the x-y nuclear center (**SFig. 7H**).

Thus, in adherent cells with flat nuclei the distance from the equatorial plane emerges as an additional key axis in nuclear genome organization in addition to the x-y plane radial position.

Discussion

Here we integrated imaging with both spatial (DamID, TSA-seq) and functional (Repli-seq, RNA-seq) genomic readouts across four human cell lines. Our results provide new insights that significantly extend previous nuclear genome organization models, while also demonstrating a cell-type dependent complexity of nuclear genome organization (**Fig. 8**).

First, across the four cell lines examined, differences in gene expression correlate primarily with differences in the genome positioning of these genes relative to nuclear speckles (**Fig. 8A**) rather than distance from the nuclear lamina and despite variations in speckle positioning relative to the nuclear lamina and nucleoli. Consistent with previous observations showing a more interior nuclear localization of genes after their activation (Bickmore, 2013; Takizawa et al., 2008), we demonstrate an inverse trend between changes in speckle and lamina distances for the small fraction of genomic regions that show significant changes in their relative speckle distances. For these regions, there is a strong bias towards increased (decreased) gene expression with decreased (increased) speckle distance. However, several-fold more genomic regions significantly change their relative lamina distances without significantly changing their speckle distances or gene expression. Similarly, LBR/LMNA DKO in K562 cells results in many genomic regions increasing or decreasing their lamina association without changes in their speckle distance or gene expression. In contrast, changes in DNA replication timing correlate with changes in positioning relative to all three nuclear locales-speckles, lamina, and nucleoli (**Fig. 8A**).

Second, Hi-C A compartment/iLADs are punctuated by strong (Type I) and weaker (Type II) speckle attachment regions which align with DNA replication initiation zones and show

elevated gene expression levels above flanking iLAD regions (**Fig. 8B**). Type I regions contain shorter, more exon-rich genes as compared to Type II regions and are more highly conserved across cell lines than Type II regions. IZs within strong speckle attachment sites replicate earlier than IZs within weak speckle attachment zones with the very earliest DNA replication foci appearing adjacent to nuclear speckles (**Fig. 8E**).

Third, Hi-C A compartment/iLADs are also punctuated by partially repressed fiLADs which retain weak lamina interaction and, in some cases, elevated nucleolar interactions. Identified as local maxima in lamina TSA-seq and/or DamID, these "p-w-v-fiLADs" comprise ~2/3 of all fiLADs across the four cell lines examined. P-w-v-fiLADs show gene expression levels intermediate between LADs and typical iLADs while retaining late or shifting to middle DNA replication timing. Only approximately 1/3 of fiLADs, identified as valleys in lamina DamID (v-fiLADs), convert to an active, early-replicating, interior chromatin state. The same fLADs across different cell lines can associate strongly with the lamina as a LAD, retain weak lamina association as a partially repressive p-w-v-fiLAD, or show a true transition to an interior, active, early DNA replicating state (**Fig. 8C**). Upon LMNA/LBR double KO, p-w-v-fiLADs shift closer to the lamina, suggesting they compete with LADs for lamina association in wt cells (**Fig. 8F**).

Fourth, we show how LAD regions showing different histone marks- either enriched in H3K9me3, H3K9me2 plus H2A.Z, H3K27me3, or none of these marks- can differentially segregate within nuclei. These results support the previous suggestion of different "flavors" of LAD regions, based on the autonomous targeting of BAC transgenes to the lamina (Bian et al., 2013). Differential nuclear localization also was recently inferred by the appearance of different Hi-C B-subcompartments, which similarly were differentially enriched in either H3K9m3,

H3K27me3, or the combination of H3K9me2 and H2A.Z (Spracklin et al., 2023). Here, our use of TSA-seq directly measures and assigns the intranuclear localization of different LAD regions to different nuclear locales.

Fifth, beyond the previously described dependence of genome organization relative to the radial axis in the x-y plane, there exists an unexpectedly high degree of nuclear polarity with respect to an orthogonal z-axis in HCT116 and HFF cells with flat nuclei (**Fig. 8D**). Strong speckle attachment regions localize closer to the equatorial plane than weak speckle attachment regions. A subset of LADs, primarily at the ends of long chromosome arms, preferentially localize at the lamina within this equatorial plane. Using SPIN states, ordered by DNA replication timing and levels of gene expression, we show that this overall nuclear polarity applies to nearly the entire genome, suggesting a corresponding overall gradient in both later DNA replication timing and lower gene expression with increased distance from the equatorial plane.

In conclusion, by examining genome organization relative to multiple nuclear locales, we were able to demonstrate a higher correlation than previously apparent between nuclear location and functions such as DNA replication timing and gene expression. We anticipate future mapping of the genome relative to additional nuclear locales will reveal a still more deterministic relationship between nuclear positioning and genome function.

Materials and methods

Cell culture

H1, HCT116, and HFF cells were cultured according to standard operation protocols established by the NIH 4D Nucleome Consortium (https://www.4dnucleome.org/cell-lines.html). K562 cells were cultured according to the ENCODE Consortium protocol (http://genome.ucsc.edu/ENCODE/protocols/cell/human/K562_protocol.pdf).

Immunostaining

Adherent cells (HCT116, HFF, and H1) were seeded on 12mm round coverslips and cultured for two days prior to immunostaining. For K562 cells, 150µl of cell suspension was added to coverslips treated with poly-L-lysine as described previously (Chen et al., 2018). All washing steps were 3 × 10 mins in Ca, Mg- free PBS at room-temperature (RT), unless specified elsewise. Cells were fixed with freshly made 2% paraformaldehyde (PFA) in PBS for 10 mins at RT and washed. Cells were permeabilized for 5 mins on ice with 1X PBS containing 0.2% Triton X-100 (Sigma-Aldrich T8787*)* and 1% natural goat serum (NGS) and washed with 1XPBS/1% NGS (PBS/NGS) 3 x 10 mins at RT. Each coverslip was then incubated with 100µl of the primary antibody cocktail in a dark humid chamber at 4˚C overnight. The cocktail contained moue-anti-RL1 (Santa Cruz cat# sc-58815, 1:100 dilution), rabbit-MKI67IP (Atlas antibodies cat# HPA035735, 4ng/ml dilution) and rabbit-anti-SON (Pacific Immunology Corp, custom-raised, 4ng/ml dilution) (Chen et al., 2018) diluted in PBS/NGS. The anti-MKI67IP and anti-SON antibodies were directly labelled with CF-594 and CF-640R fluorophores using Mix-n-Stain™ CF® Dye Antibody Labeling Kits (Biotium cat #92256 and #92258) according to manufacturer's

instructions. After immunostaining, coverslips were washed and RL1 antibody was immunostained with goat-anti-mouse-Alexa-Fluor-488 secondary antibody (Jackson ImmunoResearch Laboratories, cat#115-545-003) diluted 1:500 in PBS/NGS) for 1 hr in a dark humid chamber at RT and washed. The DNA was counterstained with 200 ng/ml DAPI in PBS for 10 mins at RT and washed. Finally, the coverslips were mounted on glass slides using an antifade mounting media (10% w/v Mowiol 4-88(EMD Millipore)/1% w/v DABCO (Sigma-Aldrich)/25% glycerol/0.1 M Tris, pH 8.5) and cured overnight before proceeding to imaging.

Microscopy and image segmentation

Locales were imaged using the OMX-V4 microscope (GE Healthcare) equipped with a U Plan S-Apo 100×/1.40-NA oil-immersion objective (Olympus), two Evolve EMCCD cameras (Photometrics). Z-sections were 125 nm apart. Images were segmented in 3D using a combination of in-house softwares and the Allen Cell and Structure Segmenter (Segmenter) toolkit in Python (Chen et al., 2020). Briefly, nuclei were first identified by segmenting DAPI using Otsu thresholding method. RL1 signal was first segmented using a modified nup153 workflow from Segmenter. In H1 cells, there are some cytoplasmic signals for RL1 which were removed using the DAPI nucleus mask. RL1 signals are puncta and the alpha-shapes algorithm (Edelsbrunner et al., 1983) was used to calculate a 3D mesh-surface enclosing all the puncta (SFig 1A). This surface was used to measure the nuclei's volume (V), surface area (SA), and SA/V. We segmented SON using the SON workflow, and MKI67IP using "masked object thresholding" workflow from Segmenter. The binary segmented images were used to measure the total number of locales in each nucleus and average and total V, SA. Nuclei images and

segmentations were manually curated for quality control and are available online. To measure locale distances in each cell line, the SON and MKI67IP binary images were converted to mesh surfaces using a marching cube algorithm. An asymmetric locale to locale distance was then calculated by measuring the closest distance between a pair of vertices from locales mesh-surfaces (SFig. 1B). The PCA analysis was performed in R using 15 numerical metrics for each nucleus (Fig. 1F and SFig. 1F).

HCT116 EGFP-SON KI

A Cas9/sgRNA RNP complex and linear dsDNA donor were transfected into HCT116 cells using the Amaxa Nucleofector II device (Lonza) set for program D-032 with the Cell Line Nucleofector Kit V. We obtained the guide and CRISPR RNA using the GeneArt Precision gRNA Synthesis Kit (Thermo Fisher Scientific) with our designed SON guide sequence 5'-gagagaacggagcggacgcca -3'. The Cas9 protein Alt-R S.p. Cas9 Nuclease V3 was purchased from Integrated DNA Technologies (IDT). Donor DNA was amplified by PCR from a previously modified version of the SON-containing BAC RP11-165J2 (Invitrogen) with EGFP sequence at the NH2 terminus of SON (Khanna et al., 2014). We used modified primers containing a 5' amine group with a C6 linker (Yu et al., 2020) 5'- GTGCTCACTGATTGGTCCCTC - 3' and 5' - GAACGACTGCGTCTCCGAAG - 3' (amC6, IDT) to obtain a 1044bp fragment that includes the EGFP sequence flanked by a 160bp upstream and a 165bp downstream homologous region of SON. After 5 days of recovery, EGFP-positive cells were sorted using the FACS ARIA II sorter at the UIUC Roy J. Carver Biotechnology Center. Individual HCT116 clones expressing SON-GFP were genotyped by PCR with primers 5'- CAAGAGAGACGGCTCCTGTAATG -3' and 5'-

TCGGAAAAGGCGAAGTTCCTCG -3' which amplify the complete EGFP integration to identify the double allele knock-in clone "C4". HCT116 EGFP-SON clone C4 was transduced with a lentivirus carrying the Lenti-mCherry-PCNA construct (Xiong et al., 2023) by supplementing media with 8 µg/ml polybrene (Santa Cruz Biotechnology).

Live-cell Imaging and analysis

HCT116 EGFP-SON clone C4 cells expressing mCherry-PCNA were seeded in 35-mm dishes with a #1.5-thickness glass coverslip bottom (MatTek, P35G-1.5-14-C) and grown to ~90% confluency. Live cell imaging was performed using a OMX V4 (Applied Precision) microscope with a 100×/1.4 NA oil immersion objective (Olympus), two Evolve EMCCDs (Photometrics), and a live-cell incubation chamber. The chamber contains a temperature control (37°C) for the incubator and the objective lens, and a humidified CO2 supply. 3D images were acquired using a z-spacing of 300nm once every 5 mins for 12 hrs. Each z-slice was imaged at 2.0% transmittance and 10ms exposure for 488nm excitation (GFP, Speckles), and 5.0% T with 10ms exposure for 568nm (mCherry, PCNA). We used FIJI to smooth images and remove noise. A median filter of 0.24µm and "rolling ball" background subtraction of ~0.5µm was used. All measurements were done from corresponding individual Z-sections per timepoint. To identify PCNA foci we used the FIJI maximum entropy threshold plugin followed by watershed segmentation of the grayscale image. FIJI's particle analysis was used to identify the center of each outlined PCNA foci, and the distance to nuclear speckle was measured from the PCNA foci center to the visible edge of the nearest nuclear speckle.

K562 LMNA and LBR single and double knock-out generation

To create LMNA and LBR knockout (KO) lines and the LMNA/LBR double knockout (DKO) line, we started with a parental K562 cell line expressing an inducible form of Cas9 (Brinkman et al., 2018). The single KO and DKO were generated according to the procedure described previously (Schep et al., 2021).

TSA-seq

SON and MKI67IP TSA-Seq was performed using Condition E (labeling with 1:300 tyramide biotin, 50% sucrose and 0.0015% hydrogen peroxide) (Zhang et al., 2020) with the following minor modification: 150ul of Dynabeads M-270 streptavidin (Invitrogen, catalog no. 65306) was used to purify the biotinylated DNA. For LMNB1 TSA-Seq, Condition A2 (Zhang et al., 2020) (labeling with 1:10000 tyramide biotin, 50% sucrose, 0.0015% hydrogen peroxide and reaction time 20 min at RT) was used.

DamID-seq and data processing

The DamID-seq and subsequent processing was performed according to a previously published protocol (Leemans et al., 2019).

RNA-seq (for K562 DKO)

RNA was isolated using the Qiagen RNeasy column purification kit, after which sequencing libraries were prepared using the Illumina TruSeq polyA stranded RNA kit.

Repli-seq and data processing (for K562 DKO)

The 2-fraction Repli-seq used in analysis of the K562 DKO cell line was done according to a previously published protocol (Marchal et al., 2018). Briefly, BrdU was added to a final concentration of 100 µM and cells were incubated at 37°C for another 2 h. Cells were fixed in ice-cold ethanol and processed for Repli-seq as described before.

Genomic segmentations

For detecting SON TSA-seq Type I and Type II peaks, the SON TSA-seq score (25 kb bins) first was smoothed using locally weighted regression (LOESS). Next, a local maximum filter with window size (w) was applied, which recorded the maximum SON TSA-seq score within this window for each genomic locus. Then the data after the maximum filter were subtracted from the original smoothed data. Peaks were retained only if they showed a reduction in value, which indicates true local peaks. A parameter optimization procedure was conducted in order to maximize the peak agreement between two SON TSA-seq replicates. As a result, a smoothing factor (span=0.005) and a window size (w=50) were selected. To distinguish local peaks into Type I and Type II, we overlapped them with Hi-C subcompartments (Rao et. al, 2014). Genomic loci overlapping A1 subcompartments were classified as Type I peaks, while those overlapping A2/B1 were designated as Type II peaks.

ROIs in H1 cells corresponding to off-diagonal 100 kb genomic bins in SON versus LMNB1 TSA-seq scatterplots were defined as those bins below the line LMNB1 = -1.5×SON – 1.3, in these scatterplots. H1 ROI genomic regions were further subdivided into H1 ROI-C1 and C2 sub-regions (Supp. Fig. 6A), in which the H1 ROI-C2 regions were defined as the genomic bins below the LMNB1= -1.5×SON – 2.2 line, while ROI-C1 regions were all remaining ROI bins.

To define LADs, p-w-v-fiLADs, and v-fiLADs, first we identified a consensus set of all chromosome regions which are LADs in at least one of the four examined cell types. Segmentation into these three domain classes was implemented heuristically using the local relative increase ("enrichment") of the domain DamID score relative to its flanking regions (**SFig. 4B**): LAD domains, defined by their positive DamID scores using a Hidden Markov model, showed the largest positive local enrichment. We defined v-fiLADs as those domains which changed from LADs in a different cell line to iLADs and which showed lower local enrichment than 95% of the LADs. P-w-v-fiLADs were then defined as all other fiLAD domains and showed intermediate local enrichment levels.

To define LAD clusters in HCT116 cells based on LMNB1 vesus SON TSA-seq scatterplots, all 100kb genomic bins corresponding to LADs based on the HCT116 DamID (4DN file) were divided into 4 quadrants (Fig. 6E) centered at SON = -3.0 and LMNB1= 0.25. The C1, C2, C3, and C4 clusters were defined as the top-left, top-right, bottom-left, and bottom right quadrants, respectively.

Equatorial (Cluster 1) and non-equatorial (Cluster 2) LADs were defined in HFF cells (Fig. 7B) as those 100 kb bins which were LADs as defined by the LMNB1 DamID which had LMNB1 TSA-seq (4DN file number) scores higher than 0.75 for the equatorial LADs or SON TSA-seq (4DN file number) scores less than 0.98 for the non-equatorial LADs.

Gene expression analysis

Regarding Fig. 6H, the genes overlapping with C1-C4 LAD clusters were identified and their expression was evaluated in HCT116 RNA-seq.

Correlations with other genomic features

Data sets used for this study (Supplementary Table 1) include TSA-seq, DamID-seq, Repli-seq, RNA-seq, ChIP-seq and HiC compartment scores. TSA-seq, DamID, Repli-seq, and ChIP-seq data were mapped to hg38 and binned in 25 kb genomic windows, except for analysis included in Fig. 6 and SFig. 6.

For the ChIP-seq analysis in Fig. 6, fold-change over input was calculated for 25kb bins and was converted to percentile values across the genome. The percentile values were averaged over all the bins corresponding to the C1-C4 LAD clusters in the Fig. 6F heatmap or were overlayed on the LMNB1 versus SON TSA-seq binned scatterplots in Fig. 6G.

A cLAD score was calculated using the DamID LAD calls in 7 available human cell lines (STable 1). First the union of all LAD calls among the 7 cell lines was computed. For each 100kb genomic bin a number between 1 to 7 was assigned depending on the number of cell lines in which the bin was called as a LAD. The average cLAD score was overlayed on the LMNB1 versus SON TSA-seq binned scatterplot in Fig. 6J.

Correlating omics data with the IMR90 multiplex FISH data

For the LMNB1 TSA simulation (Fig. 7A), a 3D image of the segmented HFF nuclear periphery (anti-RL1 staining) was used. The binary image was convolved with a symmetrical 3D kernel based on the exponential decay function, Be^{-R*d}, of the TSA-biotin signal in which R is the decay constant and d is the distance to the central element of the kernel (B= 5.86, R= 3).

To correlate HFF LAD clusters with the FISH data from Su et al. (Su et al., 2020) (Fig. 7C-D) the x-y coordinates of FISH probes were first rotated using Principal Component Analysis (PCA) such that the length (PC1) and width (PC2) of each nucleus aligns with its PC1 (X) and PC2 (Y) axes. The size of each nucleus was then normalized to fit in a 4x2x1 (X*Y*Z, arbitrary units) cuboid using a min-max normalization. Probes mapping within equatorial (EQ, Cluster 1) and non-equatorial (non-EQ, Cluster 2) LAD clusters were selected and overlayed to generate Fig. 7C. Similarly, to correlate high-throughput FISH data with distance to centromeres, probes mapping to chromosome 4 (Fig. 7D) were selected and their distances to centromeres were calculated using UCSC chromosome banding data (STable 1).

Data access and code availability

Bed files corresponding to the genomic domains and datasets that we are uploading or previously have uploaded to 4DN can be found on the manuscript webpage on the 4DN website (https://data.4dnucleome.org/belmont_lab_nuclear_locale).

The K562 LMNA, LBR, and LMNA/LBR DamID-seq, Repli-seq, and RNA-seq raw and processed data has been deposited to GEO (GSE263012). The locale imaging data and the corresponding segmentations can be found on Illinois Data Bank (https://doi.org/10.13012/B2IDB-9792611_V1). The code used to generate figures in this manuscript, along with processed input and output files can be found have been reposited to the Illinois Data Bank (https://doi.org/10.13012/B2IDB-4383352_V1).

Acknowledgements:

This work was supported by the National Institutes of Health Common Fund 4D Nucleome Program grants U54DK107965 (A.S.B., B.v.S., D.M.G., and J.M.) and UM1HG011593 (J.M., A.S.B., and D.M.G.). Research at the Netherlands Cancer Institute is supported by an institutional grant of the Dutch Cancer Society and of the Dutch Ministry of Health, Welfare and Sports. The Oncode Institute is partially funded by the Dutch Cancer Society.

Author contributions:

OG, TvS, YW, PK, LZ, YZ are co-first authors based on their contributions described below. This study was a highly collaborative group effort between the laboratories of ASB, BvS, DMG, and JM as a research center during the of NIH's 4D-Nucleome's consortium phase I. The analysis performed here were led by two PhD students, OG and TvS from the laboratories of ASB and BsV, respectively. They organized weekly online meetings among all the trainees with monthly guidance from the corresponding authors.

Data gathering: OG (HCT116 and K562) and PK (H1, HFF and K562-LMNA/LBR DKO) performed the immunofluorescence staining of locales and collected images. LZ (HCT116, H1 and HFF) and PK (K562, H1 and HFF) performed LMNB1 TSA-seq experiments. PK performed and processed MKI67IP TSA-seq experiments. PK performed MKI67IP, LMNB1 and SON TSA-seq in K562 WT and K562-LMNA/LBR DKO cell lines. TvS performed LMNB1 DamID experiments. AEV performed the early/late repli-seq in K562-LMNA/LBR DKO cell lines. YZ and YW curated and performed quality control on RNA- and ChIP-seq datasets from external sources. They also created the

infrastructure needed for organization and hosting of data generated for this study and external data for trainees to use.

Hypothesis generation and analysis: All authors contributed to hypothesis generation with the following specifics. OG created software for the segmentation and the analysis of nuclear locales microscopy data (Fig. 1 and Supp. Fig. 1). TvS performed most of the analysis for Fig. 2 and supp. Fig. 2. LZ performed analysis for Fig. 2C and SFig. 2D-E. YW performed most of the analysis for Fig. 3 and SFig. 3. PAZ performed the initial analysis for Fig. 3F, which was then reproduced by YW. GAHG performed live-cell imaging and the analysis of related to SFig. 3F. Initial idea for p-w-v fiLADS (Fig. 4) was developed by PK and ASB which was then realized in Fig. 4 and supp. Fig. 4 by analysis done by TvS. Analysis in Fig. 5 and supp. Fig. 5 were done by TvS. Analysis in Fig. 6 and supp. Fig. 6 were done by OG. Analysis in Fig. 7 and supp. Fig. 7 were done by OG and TvS. Ideas behind Fig. 8 were developed by OG and ASB and was realized by OG.

Writing: Original draft was written by OG, TvS, YW, and ASB. Later drafts and final manuscript were written by OG and ASB with inputs from others.

Figure Legends:

Figure 1: Differences in nuclear and nuclear body morphology and relative positioning among four cell types. (**A-B**) Wide-field deconvolution light microscopy (**A**) and 3D solid models in XY and XZ orientations (**B**). Immunostaining of nuclear periphery (NP), nucleoli, and nuclear speckles using antibodies against RL1 (nuclear pore, purple), MKI67IP (nucleolar GC, orange), and SON (nuclear speckle, green) in H1, K562, HCT116, and HFF cells. (**C**) Comparing Volume (V), surface area (SA), and roundness (SA/V) of nuclei measured from NP 3D solid models in H1 (red), K562 (blue), HCT116 (green), and HFF (yellow) cells. (**D**) Comparison across cell lines of nucleolar and nuclear speckle (NS) numbers, average volumes, and summed volumes per nucleus. Individual NS are significantly larger in HCT116 cells, even though total NS volumes are similar across all four cell lines. (**E**) Pairwise average distances between locales (asymmetric, as defined in SFig. 1B). (**F**) Principal Component (PC) 1 (x-axis) versus PC2 (y-axis) scatterplot using PCA of 14 morphological features reveals adjacent clustering of H1 and K562 cells with HCT116 and HFF clusters closer to each than to H1 and K562 cells. Each scatterplot point represents an individual cell. Arrow lengths show the quality of representation and arrow direction show the loadings on PC1 and PC2.

Figure 2: Global changes in nuclear genome intranuclear positioning and their correlations with changes in gene expression and DNA replication timing. (**A**) Chr1 left arm browser view suggests chromosome trajectory alternating between positioning of early replicating regions near nuclear speckles and late-replicating regions at either the nucleolar (H1, K562) or the nuclear periphery (HCT116, HFF); Top to bottom- nuclear speckle (SON, green), Nucleolus

(MKI67IP, orange), and nuclear lamina (LMNB1, purple) TSA-seq, LMNB1 (purple) DamID, and 2-fraction Repli-seq (Replication timing, brown). Left to right- H1, K562, HCT116, and HFF cells. (**B**) Comparison of Pearson correlations of TSA-seq and DamID datasets between different cell lines (H1,K562,HCT116, HFF) reveals much higher conservation of genome positioning relative to nuclear speckles, which is largely conserved, versus nucleoli or nuclear lamina; (**C**) Left- Genes positioned closer (blue)/ further (red) to nuclear speckles show a bias towards increased / decreased gene expression in HFF versus H1 cells. Gene fraction (x-axis) versus log2 FKPM (HFF/H1) (y-axis); Right- Similar comparison for genes positioned closer (blue) / further (red) to nuclear lamina does not show such bias; (**D-E**) Changes in gene expression between H1 and HFF cells vary largely as function of changes in nuclear speckle rather than nuclear periphery or nucleolar relative positioning; (**D**) 2D histograms showing mean ratio changes in gene expression between H1 versus HFF cells (log2 ratios of FKPM, color-coded) for binned genes as function of their changes in z-normalized TSA-seq scores (left to right: LMNB1 (y) vs SON (x), MKI67IP (y) vs SON (x), MKI67IP (y) vs LMNB1 (x)); (**E**) Linear modeling of changes in gene expression versus z-normalized TSA-seq score changes reveals significantly larger coefficients (dependence) for SON (green) versus MKI67IP (orange) or LMNB1 (blue). (**F-G**) Similar comparison as in (D-E), but for replication timing (2-fraction Repli-seq), shows changes in DNA replication timing are function of both changes in SON and LMNB1 TSA-seq.

Figure 3: Varying gene composition, DNA replication timing, and speckle proximity of Type I versus Type II SON TSA-seq peaks which align with gene expression "hot-zones" and DNA replication initiation zones (IZs). (**A**) SON TSA-seq Type I (red ticks) and Type II (blue ticks) local

maxima ("peaks") align with DNA early replication IZs identified in 16-fraction (S1 (early) – S16 (late)) Repli-seq. Top to bottom: K562 SON TSA-seq, HCT116 SON TSA-seq and Repli-seq, H1 SON TSA-seq and Repli-seq, HFF SON TSA-seq; (**B-C**) Histograms of distances (x-axis, nm) (**B**) and boxplots showing speckle association fractions (<250 nm) (**C)** of HFF Type I and II peaks located in IMR90 fibroblasts [43] from nuclear speckles show higher and unimodal (Type I) versus lower and bimodal (Type II) nuclear speckle attachment frequencies ; (**D**) Pileup plots showing SON TSA-seq (left), Repli-seq (2nd to left), FKPM RNA-seq (2nd from right), and Hi-C compartment scores (right) flanking (+/- 500 kb) Type I (red) versus Type II (blue) SON TSA-seq peaks; (**E**) Boxplots of Trep (timing of replication, left) and Twidth (variation in replication timing, right) in H1 (top) and HCT116 (bottom) show earlier and less variable DNA replication timing for Type I versus II peaks; (**F**) Pileup Repli-seq profiles for early, early-mid, late-mid, and late IZs (left, +/- 1 Mbp) show progressively later timing of replication correlating with the lower amplitude of SON TSA-seq peaks (right) centered at the IZ center (right).

Figure 4: Facultative LADs transition most frequently to a partially repressed, middle-to-late replicating iLAD and less frequently to an active, early replicating facultative iLAD in different cell types. (**A**) Chr1 region with examples of LADs (red rectangles) showing peaks in LMNB1 DamID in one cell type changing in other cell types to facultative iLADs (fiLADs) showing either valleys ("v") (blue rectangles) or peak-within-valleys ("p-w-v") (yellow-orange rectangles) in their LMNB1 DamID signals. Replication timing is late for fLADs, changes to early for v-fiLADs but remains late-to-middle for p-w-v fiLADs, despite Hi-C A compartment scores for both p-w-v and v-fiLADs . Top to bottom - LMNB1 DamID for H1, HCT116, K562, and HFF, Hi-C A/B

Eigenvector score for H1 and HCT116, 16-fraction Repli-seq for H1 and HCT116, and 2-fraction Repli-Seq for K562 and HFF (H1-red; HCT116-green; K562-blue; HFF-brown) (some v-fiLADs and iLADs are p-w-v fiLADs classified as v-fiLADs or missed by our classification scheme); (**B-C**) Numbers (**B**) and mean sizes (**C**) of LADs (red), p-w-v fiLADs (yellow/orange), and v-fiLADs (blue) in the four cell types. HFF cells have smallest number of p-w-v and v fiLADs; (**D**) Genes in same domain type show similar expression mean levels but show increased expression in p-w-v fiLADs versus LADs or v fiLADs versus p-w-v fiLADs in H1 versus HCT116. Log2 (FKPM(H1)+1 / FKPM(HCT116)+1) for genes in one type of domain in H1 and the same or another type of domain in HCT116 (H1 domain type : HCT116 domain type); (**E**) Pileup plots for LMNB1 DamID (top), E/L 2-fraction Repli-seq (middle), and Hi-C compartment score (bottom) for LADs (red), p-w-v fiLADs (yellow/orange), v fiLADs (blue) in H1 (left) versus HCT116 (right) reveals overall trend towards higher LMNB1 DamID signal, less early replication timing, and lower Hi-C compartment score of p-w-v fiLADs versus v fiLADs which resemble flanking iLAD regions; (F) 16-fraction Repli-seq pileup plots of LADs (top), p-w-v fiLADs (middle), and v fiLADs (bottom) confirms late, middle, versus early DNA replication patterns, respectively, for these domains in both H1 (left) and HCT116 (right).

Figure 5: LADs shift towards nuclear interior but peak-within-valley (p-w-v) fiLADs shift towards nuclear lamina and replicate later in LMNA/LBR double knockout (DKO) K562 cells. (**A**) Representative deconvolved widefield images showing wildtype (WT) and DKO K562 cells. Scale bar = 1 μm. DNA staining (DAPI, grey) shows increased numbers of condensed chromatin foci (arrowheads) at nucleolar (orange) periphery as well as within the nuclear interior in DKO

(middle and bottom rows) versus WT (top row) nuclei. DKO nuclei also are rounder and less lobular than wt nuclei; (**B**) Browser views over Chr1 left arm showing differences in (top to bottom) LMNB1 DamID, LMNB1, MKI67IP (nucleolar), and SON (nuclear speckle) TSA-seq, and 2-fraction Repli-seq (Early (E) / Late (L)) for WT (black) versus DKO (red) cells. Whereas LADs shift towards the nuclear interior, p-w-v fiLADs shift towards the nuclear lamina, or become actual LADs, with slightly later replication timing; in contrast, there is no significant change in nuclear speckle positioning. (**C**) Chromosome shifts away from (towards) nuclear lamina are inversely correlated with shifts towards (away from) nucleoli: 2D- histogram showing changes (KO – wt) in LMNB1 (x-axis) versus MKI67IP (y-axis) TSA-seq. For each histogram bin (pixel), the number of overlapping 25 kb genomic bins is grey-scale coded. Only pixels with at least 10 overlapping genomic bins are plotted. Pearson correlation = -0.58; (**D-E**) H3K9me3-enriched regions shift away from nuclear periphery and towards nucleoli whereas H3K27me3-enriched regions shift towards nuclear periphery and away from nucleoli in DKO versus wt cells; 2D histograms from (C) overlaid with mean wt H3K9me3 (**D**) or H3K27me3 (**E**) ChIP-seq color-coded values. (**F**) Upset plot showing numbers of differentially expressed genes in each of the 3 KO cell lines and overlap of these differentially expressed genes between KO lines; (**G**) No trend in gene expression changes as a function of increased or decreased nuclear lamin association after DKO: Scatterplot of gene expression differences (log2-ratio FKPM, y-axis) versus differences in LMNB1 DamID (x-axis) (DKO-wt). Only active genes are shown (blue, upregulated; red, downregulated; grey, no change); (**H**) Domains that shift closer to nuclear lamina in DKO cells also shift to later DNA replication: Scatterplot comparing mean changes over chromosome domains in E/L 2-fraction Repli-seq (DKO – wt) (y-axis) versus changes in LMNB1 TSA-seq (DKO –

wt) (x-axis). Domain data points are colored based on their transition class (see text) (wt LADs, p-w-v fiLADs, and v-fiLADs, and DKO fLADs).

Figure 6. Spatial segregation within nuclei of different heterochromatin types revealed by LMNB1 and SON TSA-seq. (**A**) Genomic ROI (ROIs C1 and C2 in SFig. 6) in H1 cells with disproportionately reduced nuclear lamina interactions (orange) which deviate from otherwise inverse correlation (green) between SON and LMNB1 TSA-seq. H1 SON(x-axis) versus LMNB1 (y-axis) TSA-seq scatterplot; (**B**) Mean TSA-seq LMNB1, MKI67IP, SON values for H1 ROI in HFF, HCT116, K562, and H1 cells (top to bottom) reveals decreased nuclear lamina but increased nucleolar proximity in H1 cells; (**C**) Most H1 ROIs are located within several Mbp of centromeres; distance (Mbp) boxplots of H1 ROIs versus other regions; (**D**) Higher enrichment of H3K9me3 versus other histone marks (mean ChIP-seq percentile values) in H1 ROIs in H1, HCT116, HFF, K562 cell lines; (**E**) Subdivision of HCT116 LAD genomic bins (100 kb) into four, color-coded clusters (C1-4) based on their SON and LMNB1 TSA-seq scores; light green points are iLAD bins; (**F**) LAD bins in C1-4 clusters show different histone marks; mean percentile ChIP-seq values of indicated histone marks for the C1-4 LAD clusters and iLADs; (**G**) H3K9me3, H3K27me3, H3K9me2, and H2AFZ (H2A.Z) (left to right) enriched regions show differential nuclear localization relative to nuclear speckles and lamina roughly paralleling C1-C4 clusters; SON versus LMNB1 TSA-seq 2D histograms of LADs. The color-code represents the average histone modification levels in each bin (iLADs, green points); (**H-I**) C1-4 LAD clusters vary functionally.

C1 especially but also C3 LAD bins have lower gene expression, later DNA replication timing (Trep), and more uniform replication timing (Twidth) than C2 and C4 LAD bins. iLAD bins have highest gene expression, earliest replication timing, but are less variable in replication timing than C2 and C4 LAD bins. Boxplot distributions for log2(FKPM) (**H**), Trep (**I**, left), and Twidth (**I**, right); (**J)** cLAD segregate spatially differentially from fLADs largely based on their greater distance to nuclear speckles (iLADs, green). Color-coded cLAD score (# cell lines out of 7 in which a HCT116 LAD bin maps within a LAD) superimposed on SON versus LMNB1 TSA-seq scatterplot.

Figure 7: Polarity of nuclear genome organization. (**A-C**) LMNB1 TSA-seq provides a readout of nuclear genome polarity in flat nuclei due to the diffusion radius of tyramide free-radicals, identifying a LAD subset preferentially localizing at the nuclear equatorial plane periphery. (A) nuclear pore immunostaining from HFF nucleus convolved with the 3D exponential decay function of TSA staining (pseudo-colored intensity) predicts higher biotin-labeling of lamina-associated chromatin lying in nuclear equatorial plane versus top or bottom of nucleus. Top (x-y cross section); bottom (x-z cross section). Pixel size = 80 nm; (B) 2D color-coded histogram showing number of LAD genomic bins with given SON (x-axis) and LMNB1 (y-axis) TSA-seq mean values in HFF. Rectangular boxes show selection of Cluster 1, with low to moderate LMNB1 and low SON TSA-seq, and Cluster 2, with the highest LMNB1 TSA-seq values, LAD bins; (C) Cluster 1 LADs preferentially localize to the equatorial plane of the nuclear periphery. Heat map showing FISH probe location density over many fibroblast (IMR90) nuclei (data from [43]) from Cluster 1 (left) versus Cluster 2 (right) LADs superimposed on normalized nuclear shape. Top: x-y

projection; bottom: x-z projection; (**D**) Distal chromosome arms also preferentially localize to equatorial plane. Same as (C) but using all the FISH probes mapped to Chr4 and color-coded by distance (averaged over probes) to centromere in Mbp; (**E**) Distance to IMR90 nucleus x-y center also varies with chromosome distance from centromeres: IMR90 multiplex FISH probes distance (y-axis) [43] from nuclear center (projected x-y plane distances) as a function of Chr5 position (x-axis). Grey- interquartile range of probe distances; blue- mean probe distance; red- smoothed mean probe distance. Bottom track- red rectangle marks centromere position, green rectangles mark Cluster 1 LADs.; (**F and G**) Overall nuclear genome polarization in fibroblasts (IMR90); (F) Boxplots of mean distance to nuclear center (projected x-y plane distance) for all probes (NA), or Type I (red) or Type II (blue) SON TSA-seq peaks; (G) Boxplots of mean distance to equatorial plane for SON TSA-seq peaks, facultative versus constitutive LADs, and SPIN states. Strong versus moderate bias of Type I (red) versus Type II (blue) HFF SON TSA-seq peaks, respectively, to locate close to x-y nuclear center (F) and near to the equatorial plane of nuclear interior (G, left panel). Facultative LADs (low cLAD scores) localize closer to equatorial plane than constitutive LADs (high cLAD scores) (G, middle panel). SPIN states show progressive trend of increased mean distances to equatorial plane from “speckle” to” interior active” to “interior repressed” and “near lamina 1”, to “near lamina 2” and “lamina” SPIN states (Wang, 2021) (G, right panel).

Figure 8. New insights into nuclear genome organization revealed by nuclear locale genome mapping. Human nucleus schematic (middle) shows nuclear speckles (NS, green), nucleolus (orange), and nuclear lamina (NL, purple). (A) Changes in the transcriptional activity of genes

(pink to purple gradient) primarily correlates with changes in their distance to nuclear speckles (green), rather than nuclear lamina or nucleolus, whereas changes in DNA replication timing (pink-purple-yellow gradient) correlates with distance to all three nuclear locales. Regions close to nuclear speckles replicate early, while regions close to nucleolus and/or nuclear lamina replicate late during S-phase. (B) Two types of speckle association domains (SPADs), with similarly elevated levels of gene expression but genes of different lengths and relative intron/exon fraction, associate with NS. Type-I SPADs, with shorter, more exon-rich genes, have higher NS association frequencies compared to Type-II SPADs, with longer, more intron-rich genes. (C) fLADs can assume at least three different chromatin states across different cell types: i) a B-compartment LAD (positive lamina DamID signal) with high NL association, low gene expression levels and late DNA replication (cell type 1); ii) an A-compartment p-w-v-fiLAD (peak-within-valley lamina DamID signal) with low NL association, intermediate gene expression and middle-to late DNA replication (cell type 2); iii) an A-compartment v-fiLAD (valley lamina DamID signal) with no NL association, high gene expression and early DNA replication (cell type 3). (D) In cells with flat nuclei, the genome is differentially organized relative to the nuclear equatorial plane: facultative heterochromatin regions are enriched near the NL within the equatorial plane, while constitutive heterochromatin regions are enriched near the NL towards the top or bottom of the nucleus. Nuclear speckles localize towards the nuclear equatorial plane and towards the nuclear center, with Type I SPADs closer than Type II SPADs to the equatorial plane and nuclear center. (E) Type I and II SPADs align with DNA replication initiation zones with the earliest-firing DNA replication initiation zones mapping to Type I SPADs and the earliest DNA replication foci appearing adjacent to NS. (F) LADs and p-w-v fiLADs compete for

NL versus nucleoli association: in a LMNA/LBR double knockout cell line, LADs shift from the NL towards nucleoli and the nuclear interior while p-w-v fiLADs shift towards the NL.

Supplementary Figure Legends:

Supplementary Figure 1: Comparisons of nuclear and nuclear body morphologies and the intranuclear relative positioning of nuclear bodies across four cell types. (A) Nuclear periphery segmentation was achieved by first segmenting the anti-RL1 nuclear pore signal, which approximated point sources, followed by fitting alpha-shapes to define the convex hull fitting this staining. We chose nuclear pore rather than nuclear lamina staining to mitigate the "missing cone" of spatial frequency along the optical axis which has the effect of attenuating signals from flat surfaces such as the nuclear lamina top and bottom surfaces [51]; (**B**) Schematic illustrating asymmetric distance metric: for example, NP (nuclear periphery) to NS (nuclear speckle) distance measurements refer to the nearest distance to a nuclear speckle from each NP surface point, whereas NS to NP distance measurements refer to the nearest distance to the NP from NS; (**C)** Inter-locale distance distributions- pairwise distances between NP, NS, and NUC (nucleolus)- compared across cell types; (**D**) Scatterplot comparisons between cell types (H1, red; K562, blue; HCT116, green, HFF, yellow) of different morphological metrics (Volume, vol; Surface Area, SA; Distance, dist; Flatness; Nucleolus, Nuc.; Nuclear speckle, NS; Nuclear periphery, NP); each scatterplot dot represents measurements from a single nucleus. (**E**) Percentage of explained variances (y-axis) for PC1-6 (x-axis) using Principal Component Analysis (PCA) of 14 morphological features from the immunofluorescence (IF) staining; (**F**) Principal Component (PC) 1 (x-axis) versus PC3 (y-axis) scatterplot reveals overall morphological similarity of H1 (red) and K562 (blue) nuclei with extensive overlap in both PC1 and PC3, with HCT116 and HFF nuclei varying from H1 and K562 in their lower PC1 values and HCT116 nuclei varying in their higher PC3 values from the nuclei in the other three cell lines. Each point in the

scatterplot represents a cell in principal component space. Arrow length shows the quality of representation and arrow direction show the loadings on PC1 and PC2.

Supplementary Figure 2: Global changes in nuclear genome intranuclear positioning and their correlations with changes in gene expression and DNA replication timing. (**A**) Chr1 left arm (0-60 Mbp) showing heterochromatin chromatin domains (orange highlights) which associate near nucleoli and away from the nuclear lamina in H1 and K562 cells but near the nuclear lamina in HCT116 and HFF cells. These heterochromatin regions are flanked by speckle-associated regions (green highlights) in all cell lines, suggesting a Chr1 left arm trajectory alternating between speckles and nucleoli in H1 and K562 cells versus between speckles and the lamina in HCT116 and HFF cells. Top to bottom: SON (green), MKI67IP (brown), and LMNB1 (blue) TSA-seq repeated for H1, K562, HCT116, and HFF cells; (**B**) Nuclear speckle-associated regions align with nucleolar TSA-seq peaks in K562 cells but nucleolar TSA-seq valleys in HCT116 cells. Top to bottom: SON (green), MKI67IP (brown), and LMNB1 (blue) TSA-seq repeated for K562 versus HCT116 cells; (**C**) Chromosome-wide pattern of increased LMNB1 TSA-seq peak amplitudes of LADs towards the ends of long chromosome arms (orange highlights) versus decreased peak amplitudes for centromere-proximal LADs (blue highlights); these differences are enhanced in HCT116 and HFF versus H1 and K562 cells. Top to bottom: Chr2 LMNB1 TSA-seq for H1 (red), K562 (blue), HCT116 (green), HFF (orange) over Chr2; (**D**) Regions shifted closer to nuclear speckles in HFF versus H1 cells on average are shifted away from the nuclear lamina, but not vice versa. Top: Peak in the summed SON TSA-seq signals over chromosome regions with significantly higher SON TSA-seq values in HFF versus H1 cells correlates with a valley in the

summed LMNB1 TSA-seq signals for these same regions. Bottom: peak in summed LMNB1 TSA-seq for regions significantly closer to the nuclear lamina in HFF versus H1 cells but little change in summed SON TSA-seq for these same regions; (**E**) Scatterplots showing overall inverse relationship between changes in SON versus LMNB1 TSA-seq in H1 versus HFF cells for chromosome regions with different positions relative to nuclear speckles (top) but small changes in SON TSA-seq for chromosome regions with different positions relative to nuclear lamina (bottom). Top- percentile-normalized SON versus LMNB1 TSA-seq for genomic bins from chromosome regions shifting closer to nuclear speckles in HFF cells. Despite an overall inverse correlation trend, there is a widespread in changed LMNB1 scores. Additionally, some bins show positive correlation between SON and LMNB1 TSA-seq. Bottom- Corresponding scatterplot for regions that shift significantly closer to nuclear lamina in HFF cells shows small changes in SON TSA-seq; (**F**) Linear modeling of changes in gene expression versus z-normalized TSA-seq score changes reveals significantly larger coefficients (dependence) for changes in SON (green) versus MKI67IP (orange) or LMNB1 (blue) TSA-seq, as modeled for genes in all genomic regions, in LADs only, in iLADs only, or in Type I versus II SON TSA-seq local maxima. “True” versus “False” tests for statistical significance are at a p=0.05 threshold.

Supplementary Figure 3: Varying gene composition, DNA replication timing, and speckle proximity of Type I and II SON TSA-seq peaks which align both with gene expression “hot-zones” and DNA replication initiation zones (IZs). (**A**) Boxplots of p-value of multimodality for Type I and II peaks (The Hartigan's dip test) supports the unimodal versus bimodal distance distributions (Fig. 3B) of Type I versus II SON TSA-seq peaks, respectively, from nuclear speckles;

(**B**) Boxplots showing different gene composition for Type I versus II SON TSA-seq peaks. Left to right: Gene length, exon length, intron length, and intro length/ exon length ratio; (**C**) Jaccard index shows greater conservation for Type I (red) versus II (blue) SON TSA-Seq peaks across the four cell lines; (**D**) Fraction of gene alleles transcriptionally active (x-axis) versus mean distance to nuclear speckles (y-axis) for Type I (red) versus II (blue) peaks, identified in HFF cells, from IMR90 cell FISH data [43] shows higher "ON" fraction for Type I genes closer to nuclear speckles; (**E**) Repli-seq fraction distribution of Type I (top) versus II (bottom) SON TSA-seq peaks in H1 (left) and HCT116 (right); (**F**) Live-cell imaging reveals earliest PCNA replication foci cluster near nuclear speckles in HCT116 cells, consistent with Type I SON TSA-seq peaks corresponding to IZs with the earliest replication timing. Left: Mid-nuclear optical z-sections at varying times (mins) after S-phase initiation defined by first appearance of PCNA foci showing PCNA foci (red, mCherry-PCNA) versus nuclear speckles (green, EGFP-SON); Right: Boxplots showing PCNA foci distance (y-axis) distributions from nuclear speckles at different times (mins) after S-phase began (x-axis). Top: statistics for nucleus 1; Bottom: statistics for foci from 5 nuclei. "X"= median. Scale bar = 2 μm.

Supplementary Figure 4: Facultative LADs transition most frequently to a partially repressed, middle-to-late replicating iLAD and less frequently to an active, early replicating iLAD in different cell types. (**A**) Chr1 distal left arm in H1 (red tracks) or HCT116 (green tracks) with examples of LADs (red rectangles) with peaks in LMNB1 DamID signals (top) in one cell type changing in other cell type to facultative iLADs (fiLADs) with either valley ("v") (blue rectangles) or peak-within-valley ("p-w-v") (yellow/orange rectangles) LMNB1 DamID signal (top). p-w-v

fiLADs appear either as peak-within-valleys or valleys in the LMNB1 TSA-seq (2nd from top). LADs appear as peak-within-valleys whereas p-w-v fiLADs appear frequently as peaks in MKI67IP (nucleolar) TSA-seq (3rd from top). SON TSA-seq (bottom) over these regions show local minimums which often are deeper for LADs versus p-w-v fiLADs; (**B**) Local differences in LMNB1 DamID (y-axis) over chromosome domain versus flanking regions are shown for fiLADs (left) versus LADs (right, red); a cutoff corresponding to the lowest 5% of LADs was used to segment v-fiLADs (blue) (below this cutoff) from p-w-v fiLADs (olive); (**C**) LAD numbers (y-axis) and their transitions to p-w-v fiLADs (olive) or v-fiLADs (blue) between H1, K562, HCT116, and HFF cell types; (**D**) Comparisons of gene expression levels in different domain types in the same and different cell lines. LADs and p-w-v fiLADs show similar ranges of expression levels, with median expression actually slightly lower in p-w-v fiLADs versus LADs in H1 cells. Compared to p-w-v fiLAD genes, genes in v-fiLADs show a higher range of gene expression levels which in turn is lower than the range of gene expression levels in iLADs. (**E**) Boxplots for ratios of gene expression levels (log2((FKPM(cell type 1) +1)/FKPM(cell type 2)+1)) for genes in one type of chromosome domain in one cell type versus another type of chromosome domain in a second cell type; (**F**) Heat map summary of DamID, TSA-seq, ChIP-seq, and Repli-seq signals over different chromatin domain types (left) and the relative signal differences comparing domains with their flanking regions.

Supplementary Figure 5: LADs shift towards nuclear interior but peak-within-valley (p-w-v) fiLADs shift towards the nuclear lamina and replicate later after LMNA/LBR double knockout (DKO). (A) Comparisons over Chr1 left arm between: (Top to bottom) LMNB1 DamID signals in wildtype (wt) K562 cells, parental clone expressing CRISPR Cas9 fused to a destabilization

domain, LBR knockout (KO) clone, LMNA KO clone, and LBR/LMNA DKO clone. Black box at right end of plots shows centromere region. (**B**) Comparisons between wt (blue tracks) and DKO (orange tracks) over left arm Chr1 for: (Top to bottom) LMNB1 DamID, 2-fraction Repli-seq (Early / Late (E/L) ratio, and LMNB1, MKI67IP, and SON TSA-seq. Rectangles highlight specific domain classes in wt K562 defined by comparison of cell types (see text and Fig. 4) (LADs, red; p-w-v fiLADs, orange; v-fiLADs, blue). Also shown are "DKO fLADs" (green rectangles) , a domain class defined as wt iLADs, not previously defined by cell type comparisons, which become LADs in the DKO; (**C**) Numbers of LADs in DKO that arise from wt LADs, p-w-v fiLADs, and v-fiLADs, and "DKO fLADs" which arise from wt iLADs; (**D**) Fraction of wt LADs, p-w-v fiLADs, and v-fiLADs that are LADs in DKO; (**E**) No trend in LAD gene expression changes as a function of increased or decreased nuclear lamin association: scatterplot of gene expression differences (log2-ratio FKPM, y-axis) versus differences in LMNB1 DamID (x-axis). Only active LAD genes are shown (blue, upregulated; red, downregulated; grey, no change); (**F**) Generation of a matched set of iLAD genes. LAD genes are expressed at lower expression levels than iLAD genes (left panel). To compare LAD and iLAD genes, we selected a matching set of iLAD genes with similar gene expression to the set of LAD genes (right panel). This was repeated 100 times for a robust result; (**G**) Fractions (y-axis) of differentially expressed genes in iLADs (grey) versus LADs (black) (defined in wt cells) in LBR KO (left), LMNA KO (middle), or DKO (right); (**H**) (Left) Differences in E/L Repli-seq ratios (y-axis) versus changes in LMNB1 TSA-seq for individual genomic bins corresponding to LADs in wt and/or DKO cells. Curve fitting through data points reveals a trend for later DNA replication timing for LAD genomic bins which shift closer to nuclear lamina in DKO; (Right) Scatterplot showing log2-ratios of gene expression levels (y-axis) versus changes

in LMNB1 TSA-seq for individual genes in LADs within wt and/or DKO cells. No consistent trend for changes in gene expression in DKO versus wt cells is observed; **(I)** Scatterplot comparing mean changes over chromosome domains in E/L 2-fraction Repli-seq (DKO – wt) (y-axis) versus changes in LMNB1 Dam-ID (DKO – wt) (x-axis) further supports trend towards later DNA replication timing for LADs, p-w-v fiLADs, and v-fiLADs which show increased association with nuclear lamina in DKO (similar to Fig. 5H comparing E/L Repli-seq to LMNB1 TSA-seq).

Supplementary Figure 6: LMNB1 and SON TSA-seq reveal differential intranuclear spatial segregation of centromeric and pericentromeric regions and LADs in different cell types. Further dividing LMNB1 versus SON TSA-seq scatterplot off-diagonal genomic bins into two Region-of-Interests (ROIs) reveals two subsets of genomic regions with low SON TSA-seq which lose nuclear lamina interactions specifically in H1 cells- the furthest off-diagonal ROI-C1 bins correspond to pericentric chromosome regions, particularly enriched on NOR-containing chromosomes, while ROI-C2 bins correspond to more distal chromosome regions flanking centromere regions. (**A**) An overall inverse relationship between LMNB1 and SON TSA-seq exists in both H1 and K562 cells creating a diagonal pattern in the LMNB (y-axis) versus SON (x-axis) TSA-seq scatterplot. Specifically in H1 cells, off-diagonal bins with low SON TSA-seq but also low LMNB1 TSA-seq appear. These were further divided into two H1 ROIs (C1, orange; C2, blue) relative to other genomic regions (green). These H1 ROI-C1 and ROI-C2 regions map to local clusters that lie within the overall LMNB1 versus SON scatterplot patterns in K562, HCT116, and HFF cells; (**B-C**) H1 C1 and C2 ROIs associate with both nucleoli and nuclear lamina in other cell lines but lose nuclear lamina association while gaining stronger nucleolar

association in H1 cells: LMNB1 (**B**) and MKI67IP (nucleolus) (**C**) TSA-seq boxplots for H1 ROI-C1 and C2 (orange) bins versus other genomic regions (green); (**D**) (Top) The LMNB1 (y-axis) versus SON (x-axis) TSA-seq scatterplot on-diagonal positions of H1 C1 and C2 ROIs in wt K562 cells (left) shift closer to the off-diagonal distribution visualized in H1 cells after LBR, LMNA double-knockout (KO) (right); (Bottom) MKI67IP (y-axis) versus SON (x-axis) TSA-seq scatterplots reveal these H1 C1 ROIs show high nucleolar associations in both wt and double knockout K562 cells; (**E**) Centromeric and pericentromeric locations of H1 ROI C1 (red), C2 (blue) segmented regions (bottom 2 tracks) shown in H1 cells for non-NOR containing Chr7 (left) and NOR-containing Chr13 (right) regions with MKI67IP (brown), SON (green), LMNB1 (blue) TSA-seq (top 3 tracks) showing high nucleolar and low nuclear speckle and lamina interactions; (**F**) Majority of LAD bins have high LMNB1 TSA-seq scores in H1 and K562 (round cells), but medium scores in HCT116 and HFF (flat cells). Distribution of LAD (blue) versus iLAD (green) genomic bins with LAD count superimposed over corresponding bins (color-coded) in LMNB1 (y-axis) and SON (x-axis) TSA-seq scatterplots for H1, K562, HCT116, and HFF cells (left to right).

Supplementary Figure 7: Polarity of nuclear genome organization. (A) HFF Cluster 1 LAD bins (green), defined by their lowest SON TSA-seq scores, show low to moderate LMNB1 TSA-seq scores in both HFF and HCT116. In contrast, HFF Cluster 2 LAD bins, defined as LAD regions with the highest LMNB1 TSA-seq scores in HFF, while also showing high LMNB1 TSA-scores in HCT116 instead show lower LMNB1 TSA-seq scores relative to HFF Cluster 1 LAD bins in both K562 and H1 cells: SON (x-axis) versus LMNB1 (y-axis) TSA-seq scatterplots color-coded by HFF Cluster 1 and 2 LADs shown for HFF, HCT116, H1, and K562 cells; (**B**) Chromosome ideograms

showing location of HFF1 Cluster 1 LAD regions, which show a bias towards the equatorial plane in IMR90 cells, towards the ends of long chromosome arms; (**C-D**) Distances to IMR90 nucleus center (**C**) and equatorial plane (**D**) vary with chromosome position, particularly distance from centromeres (dashed vertical lines): IMR90 multiplex FISH probe distances [43] from center and equatorial plane along each chromosome. Grey- interquartile range of probe positions; blue- mean probe position distance; red- smoothed mean probe distance. Ends of long chromosome arms, and chromosome arm regions containing Cluster 1 LADs, show trend of localizing away from nuclear center but close to equatorial plane; **(E)** Projection of IMR90 FISH probe distances (color-coded) from nuclear speckles (left), nucleoli (middle), and nuclear periphery (right) from a single nucleus onto the x-y plane (top) or x-z plane (bottom); (**F**) Scatterplots of mean distance from equatorial plane (y-axis) and from nuclear center (x-axis) of FISH probes in IMR90 nuclei with the mean distance in IMR90 nuclei (top) or mean TSA-seq scores in HFF nuclei of same FISH probe regions relative to the nuclear lamina (left), nucleolus (middle), or nuclear speckle (right) (FISH probe distances from [43]); (**G-I**) Scatterplots similar to (F) but color-coded with the genomic classification of each FISH probe: type I/II SPADs (**G**), LADs, p-w-v fILADs, v-fiLADs, iLADs (**H**, left panel), SPIN states (**I**). (**H, middle and right panels)** Boxplots for IMR90 mean FISH probe distances to nuclear center (middle panel) or nuclear equatorial plane (right panel) for HFF LADs, p-w-v fiLADs, v-fiLADs, and iLAD regions.

References:

Belmont AS. 2022. Nuclear Compartments: An Incomplete Primer to Nuclear Compartments, Bodies, and Genome Organization Relative to Nuclear Architecture. *Cold Spring Harb Perspect Biol* **14**. doi:10.1101/cshperspect.a041268

Bernhard W, Granboulan N. 1963. The Fine Structure of the Cancer Cell Nucleus. *Exp Cell Res* **24**:SUPPL9:19-53. doi:10.1016/0014-4827(63)90243-x

Bian Q, Khanna N, Alvikas J, Belmont AS. 2013. beta-Globin cis-elements determine differential nuclear targeting through epigenetic modifications. *J Cell Biol* **203**:767–83. doi:10.1083/jcb.201305027

Bickmore WA. 2013. The spatial organization of the human genome. *Annu Rev Genomics Hum Genet* **14**:67–84. doi:10.1146/annurev-genom-091212-153515

Brinkman EK, Chen T, de Haas M, Holland HA, Akhtar W, van Steensel B. 2018. Kinetics and Fidelity of the Repair of Cas9-Induced Double-Strand DNA Breaks. *Mol Cell* **70**:801-813.e6. doi:10.1016/j.molcel.2018.04.016

Chen J, Ding L, Viana MP, Lee H, Sluezwski MF, Morris B, Hendershott MC, Yang R, Mueller IA, Rafelski SM. 2020. The Allen Cell and Structure Segmenter: a new open source toolkit for segmenting 3D intracellular structures in fluorescence microscopy images. doi:10.1101/491035

Chen Y, Zhang Y, Wang Y, Zhang L, Brinkman EK, Adam SA, Goldman R, van Steensel B, Ma J, Belmont AS. 2018. Mapping 3D genome organization relative to nuclear compartments using TSA-Seq as a cytological ruler. *J Cell Biol* **217**:4025–4048. doi:10.1083/jcb.201807108

Cremer T, Cremer C. 2006. Rise, fall and resurrection of chromosome territories: a historical perspective. Part I. The rise of chromosome territories. *Eur J Histochem* **50**:161–76.

Cremer T, Cremer M, Hubner B, Strickfaden H, Smeets D, Popken J, Sterr M, Markaki Y, Rippe K, Cremer C. 2015. The 4D nucleome: Evidence for a dynamic nuclear landscape based on co-aligned active and inactive nuclear compartments. *FEBS Lett* **589**:2931–43. doi:10.1016/j.febslet.2015.05.037

Croft JA, Bridger JM, Boyle S, Perry P, Teague P, Bickmore WA. 1999. Differences in the localization and morphology of chromosomes in the human nucleus. *J Cell Biol* **145**:1119–31.

Edelsbrunner H, Kirkpatrick D, Seidel R. 1983. On the shape of a set of points in the plane. *IEEE Transactions on Information Theory* **29**:551–559. doi:10.1109/TIT.1983.1056714

Girelli G, Custodio J, Kallas T, Agostini F, Wernersson E, Spanjaard B, Mota A, Kolbeinsdottir S, Gelali E, Crosetto N, Bienko M. 2020. GPSeq reveals the radial organization of chromatin in the cell nucleus. *Nat Biotechnol* **38**:1184–1193. doi:10.1038/s41587-020-0519-y

Guelen L, Pagie L, Brasset E, Meuleman W, Faza MB, Talhout W, Eussen BH, de Klein A, Wessels L, de Laat W, van Steensel B. 2008. Domain organization of human chromosomes revealed by mapping of nuclear lamina interactions. *Nature* **453**:948–51.

Hartigan JA, Hartigan PM. 1985. The Dip Test of Unimodality. *The Annals of Statistics* **13**:70–84. doi:10.1214/aos/1176346577

Kind J, Pagie L, Ortabozkoyun H, Boyle S, de Vries SS, Janssen H, Amendola M, Nolen LD, Bickmore WA, van Steensel B. 2013. Single-cell dynamics of genome-nuclear lamina interactions. *Cell* **153**:178–92. doi:10.1016/j.cell.2013.02.028

Kolbl AC, Weigl D, Mulaw M, Thormeyer T, Bohlander SK, Cremer T, Dietzel S. 2012. The radial nuclear positioning of genes correlates with features of megabase-sized chromatin domains. *Chromosome Res* **20**:735–52. doi:10.1007/s10577-012-9309-9

Kupper K, Kolbl A, Biener D, Dittrich S, von Hase J, Thormeyer T, Fiegler H, Carter NP, Speicher MR, Cremer T, Cremer M. 2007. Radial chromatin positioning is shaped by local gene density, not by gene expression. *Chromosoma* **116**:285–306.

Leemans C, van der Zwalm MCH, Brueckner L, Comoglio F, van Schaik T, Pagie L, van Arensbergen J, van Steensel B. 2019. Promoter-Intrinsic and Local Chromatin Features Determine Gene Repression in LADs. *Cell* **177**:852-864 e14. doi:10.1016/j.cell.2019.03.009

Lieberman-Aiden E, van Berkum NL, Williams L, Imakaev M, Ragoczy T, Telling A, Amit I, Lajoie BR, Sabo PJ, Dorschner MO, Sandstrom R, Bernstein B, Bender MA, Groudine M, Gnirke A, Stamatoyannopoulos J, Mirny LA, Lander ES, Dekker J. 2009. Comprehensive mapping of long-range interactions reveals folding principles of the human genome. *Science* **326**:289–93.

Marchal C, Sasaki T, Vera D, Wilson K, Sima J, Rivera-Mulia JC, Trevilla-García C, Nogues C, Nafie E, Gilbert DM. 2018. Genome-wide analysis of replication timing by next-generation sequencing with E/L Repli-seq. *Nat Protoc* **13**:819–839. doi:10.1038/nprot.2017.148

Misteli T. 2020. The Self-Organizing Genome: Principles of Genome Architecture and Function. *Cell* **183**:28–45. doi:10.1016/j.cell.2020.09.014

Nemeth A, Conesa A, Santoyo-Lopez J, Medina I, Montaner D, Peterfia B, Solovei I, Cremer T, Dopazo J, Langst G. 2010. Initial genomics of the human nucleolus. *PLoS Genet* **6**:e1000889. doi:10.1371/journal.pgen.1000889

Peric-Hupkes D, Meuleman W, Pagie L, Bruggeman SW, Solovei I, Brugman W, Graf S, Flicek P, Kerkhoven RM, van Lohuizen M, Reinders M, Wessels L, van Steensel B. 2010. Molecular maps of the reorganization of genome-nuclear lamina interactions during differentiation. *Molecular cell* **38**:603–13. doi:10.1016/j.molcel.2010.03.016

Politz JC, Scalzo D, Groudine M. 2013. Something silent this way forms: the functional organization of the repressive nuclear compartment. *Annu Rev Cell Dev Biol* **29**:241–70. doi:10.1146/annurev-cellbio-101512-122317

Politz JCR, Scalzo D, Groudine M. 2016. The redundancy of the mammalian heterochromatic compartment. *Curr Opin Genet Dev* **37**:1–8. doi:10.1016/j.gde.2015.10.007

Quinodoz SA, Jachowicz JW, Bhat P, Ollikainen N, Banerjee AK, Goronzy IN, Blanco MR, Chovanec P, Chow A, Markaki Y, Thai J, Plath K, Guttman M. 2021. RNA promotes the formation of spatial compartments in the nucleus. *Cell* **184**:5775-5790.e30. doi:10.1016/j.cell.2021.10.014

Quinodoz SA, Ollikainen N, Tabak B, Palla A, Schmidt JM, Detmar E, Lai MM, Shishkin AA, Bhat P, Takei Y, Trinh V, Aznauryan E, Russell P, Cheng C, Jovanovic M, Chow A, Cai L, McDonel P, Garber M, Guttman M. 2018. Higher-Order Inter-chromosomal Hubs Shape 3D Genome Organization in the Nucleus. *Cell* **174**:744-757 e24. doi:10.1016/j.cell.2018.05.024

Rao SS, Huntley MH, Durand NC, Stamenova EK, Bochkov ID, Robinson JT, Sanborn AL, Machol I, Omer AD, Lander ES, Aiden EL. 2014. A 3D Map of the Human Genome at Kilobase

Resolution Reveals Principles of Chromatin Looping. *Cell* **159**:1665–80. doi:10.1016/j.cell.2014.11.021

Ryba T, Hiratani I, Lu J, Itoh M, Kulik M, Zhang J, Schulz TC, Robins AJ, Dalton S, Gilbert DM. 2010. Evolutionarily conserved replication timing profiles predict long-range chromatin interactions and distinguish closely related cell types. *Genome Res* **20**:761–70. doi:10.1101/gr.099655.109

Schep R, Brinkman EK, Leemans C, Vergara X, van der Weide RH, Morris B, van Schaik T, Manzo SG, Peric-Hupkes D, van den Berg J, Beijersbergen RL, Medema RH, van Steensel B. 2021. Impact of chromatin context on Cas9-induced DNA double-strand break repair pathway balance. *Mol Cell* **81**:2216-2230.e10. doi:10.1016/j.molcel.2021.03.032

Spracklin G, Abdennur N, Imakaev M, Chowdhury N, Pradhan S, Mirny LA, Dekker J. 2023. Diverse silent chromatin states modulate genome compartmentalization and loop extrusion barriers. *Nat Struct Mol Biol* **30**:38–51. doi:10.1038/s41594-022-00892-7

Su JH, Zheng P, Kinrot SS, Bintu B, Zhuang X. 2020. Genome-Scale Imaging of the 3D Organization and Transcriptional Activity of Chromatin. *Cell* **182**:1641-1659 e26. doi:10.1016/j.cell.2020.07.032

Takizawa T, Meaburn KJ, Misteli T. 2008. The meaning of gene positioning. *Cell* **135**:9–13. doi:10.1016/j.cell.2008.09.026

van Koningsbruggen S, Gierlinski M, Schofield P, Martin D, Barton GJ, Ariyurek Y, den Dunnen JT, Lamond AI. 2010. High-resolution whole-genome sequencing reveals that specific chromatin domains from most human chromosomes associate with nucleoli. *Mol Biol Cell* **21**:3735–48. doi:10.1091/mbc.E10-06-0508

van Schaik T, Vos M, Peric-Hupkes D, Hn Celie P, van Steensel B. 2020. Cell cycle dynamics of lamina-associated DNA. *EMBO Rep* **21**:e50636. doi:10.15252/embr.202050636

van Steensel B, Belmont AS. 2017. Lamina-Associated Domains: Links with Chromosome Architecture, Heterochromatin, and Gene Repression. *Cell* **169**:780–791. doi:10.1016/j.cell.2017.04.022

Vertii A, Ou J, Yu J, Yan A, Pages H, Liu H, Zhu LJ, Kaufman PD. 2019. Two contrasting classes of nucleolus-associated domains in mouse fibroblast heterochromatin. *Genome Res* **29**:1235–1249. doi:10.1101/gr.247072.118

Wang Y. 2021. Computational Methods for Integrative Analysis of Nuclear Genome Compartmentalization. *Computational Biology Department, Carnegie Mellon University*. Cernegie Mellon University.

Wang Y, Zhang Y, Zhang R, van Schaik T, Zhang L, Sasaki T, Peric-Hupkes D, Chen Y, Gilbert DM, van Steensel B, Belmont AS, Ma J. 2021. SPIN reveals genome-wide landscape of nuclear compartmentalization. *Genome Biol* **22**:36. doi:10.1186/s13059-020-02253-3

White EJ, Emanuelsson O, Scalzo D, Royce T, Kosak S, Oakeley EJ, Weissman S, Gerstein M, Groudine M, Snyder M, Schubeler D. 2004. DNA replication-timing analysis of human chromosome 22 at high resolution and different developmental states. *Proc Natl Acad Sci U S A* **101**:17771–6. doi:10.1073/pnas.0408170101

Xiong X, Tasan I, Yang C, Zhang M, Hernandez Gonzalez GA, Liu S, Chaturvedi P, Belmont AS, Zhao H. 2023. Imaging Method Using CRISPR/dCas9 and Engineered gRNA Scaffolds Can Perturb Replication Timing at the HSPA1 Locus. *ACS Synth Biol* **12**:1424–1436. doi:10.1021/acssynbio.2c00433

Zhang L, Zhang Y, Chen Y, Gholamalamdari O, Wang Y, Ma J, Belmont AS. 2020. TSA-seq reveals a largely conserved genome organization relative to nuclear speckles with small position changes tightly correlated with gene expression changes. *Genome Res*. doi:10.1101/gr.266239.120

Zhao PA, Sasaki T, Gilbert DM. 2020. High-resolution Repli-Seq defines the temporal choreography of initiation, elongation and termination of replication in mammalian cells. *Genome Biol* **21**:76. doi:10.1186/s13059-020-01983-8

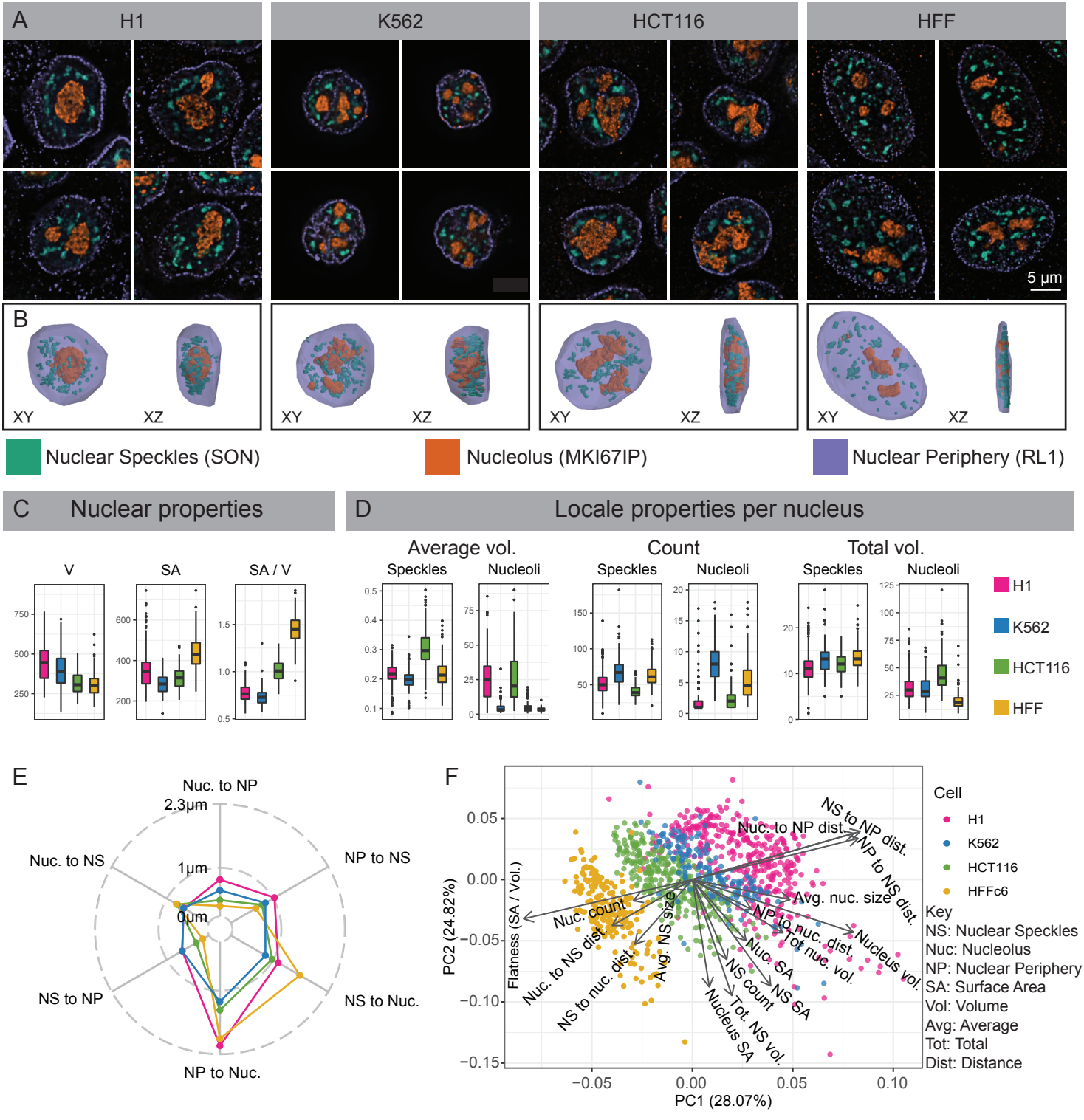
A
H1
K562
HCT116
HFF
5 µm
B
XY
XZ
Nuclear Speckles (SON)
Nucleolus (MKI67IP)
Nuclear Periphery (RL1)
C
Nuclear properties
V
SA
SA / V
D
Locale properties per nucleus
Average vol.
Count
Total vol.
Speckles
Nucleoli
H1
K562
HCT116
HFF
E
Nuc. to NP
2.3µm
1µm
0µm
NP to NS
NS to Nuc.
NP to Nuc.
NS to NP
Nuc. to NS
F
PC2 (24.82%)
PC1 (28.07%)
Flatness (SA / Vol.)
Nuc. to NP dist.
NS to NP dist.
NP to NS dist.
Avg. nuc. size
Nucleus vol.
NP to nuc. dist.
Tot nuc. vol.
Nuc. SA
NS SA
NS count
Tot. NS vol.
Nucleus SA
Avg. NS size
Nuc. count
Nuc. to NS dist.
NS to nuc. dist.
Cell
H1
K562
HCT116
HFFc6
Key
NS: Nuclear Speckles
Nuc: Nucleolus
NP: Nuclear Periphery
SA: Surface Area
Vol: Volume
Avg: Average
Tot: Total
Dist: Distance

Figure 1

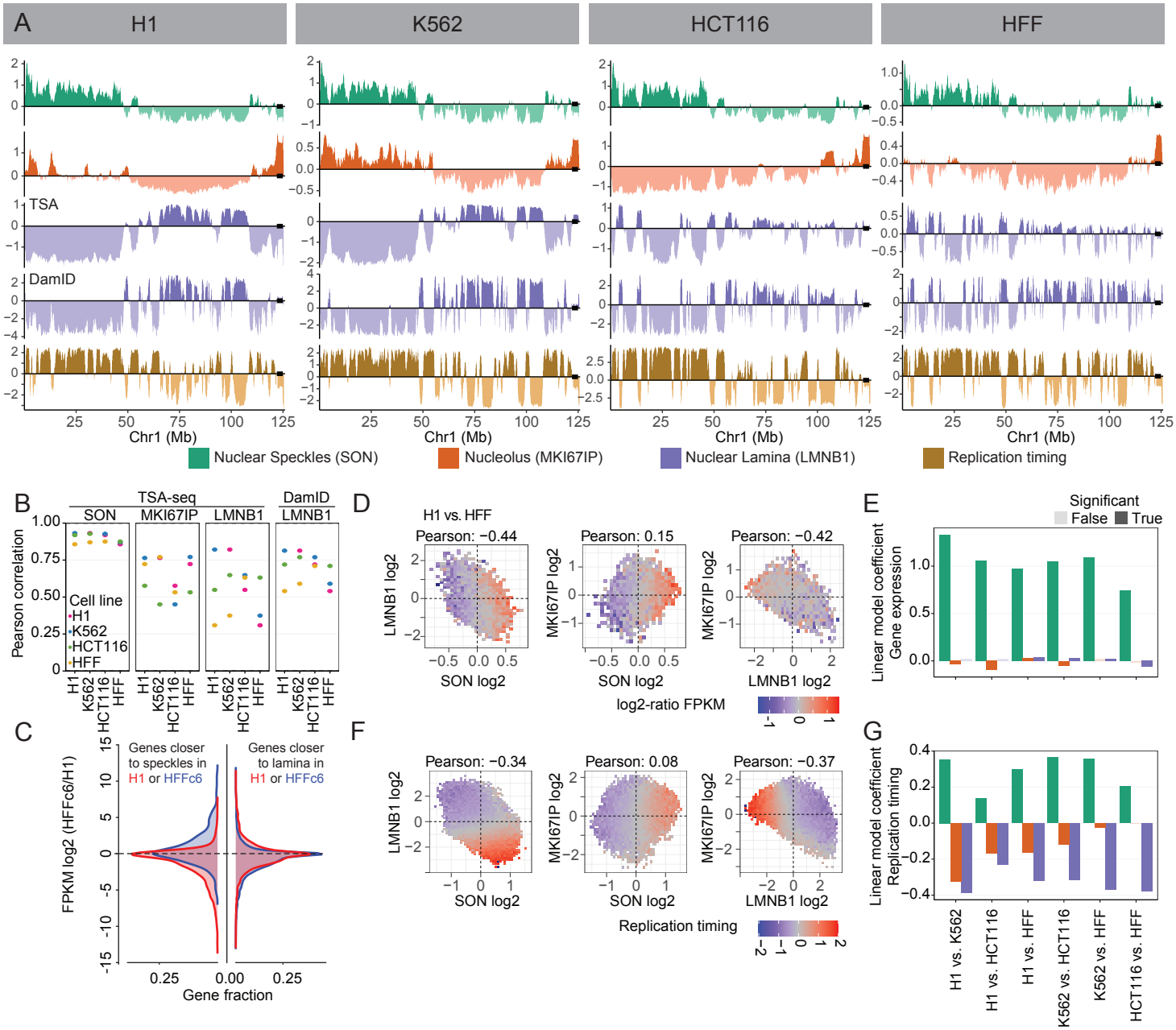
A
H1
K562
HCT116
HFF
TSA
DamID
Chr1 (Mb)
Nuclear Speckles (SON)
Nucleolus (MKI67IP)
Nuclear Lamina (LMNB1)
Replication timing
B
TSA-seq
DamID
SON
MKI67IP
LMNB1
LMNB1
Pearson correlation
Cell line
H1
K562
HCT116
HFF
C
Genes closer to speckles in H1 or HFFc6
Genes closer to lamina in H1 or HFFc6
FPKM log2 (HFFc6/H1)
Gene fraction
D
H1 vs. HFF
Pearson: −0.44
Pearson: 0.15
Pearson: −0.42
LMNB1 log2
MKI67IP log2
SON log2
LMNB1 log2
log2-ratio FPKM
E
Significant
False
True
Linear model coefficient
Gene expression
F
Pearson: −0.34
Pearson: 0.08
Pearson: −0.37
LMNB1 log2
MKI67IP log2
SON log2
LMNB1 log2
Replication timing
G
Linear model coefficient
Replication timing
H1 vs. K562
H1 vs. HCT116
H1 vs. HFF
K562 vs. HCT116
K562 vs. HFF
HCT116 vs. HFF

Figure 2

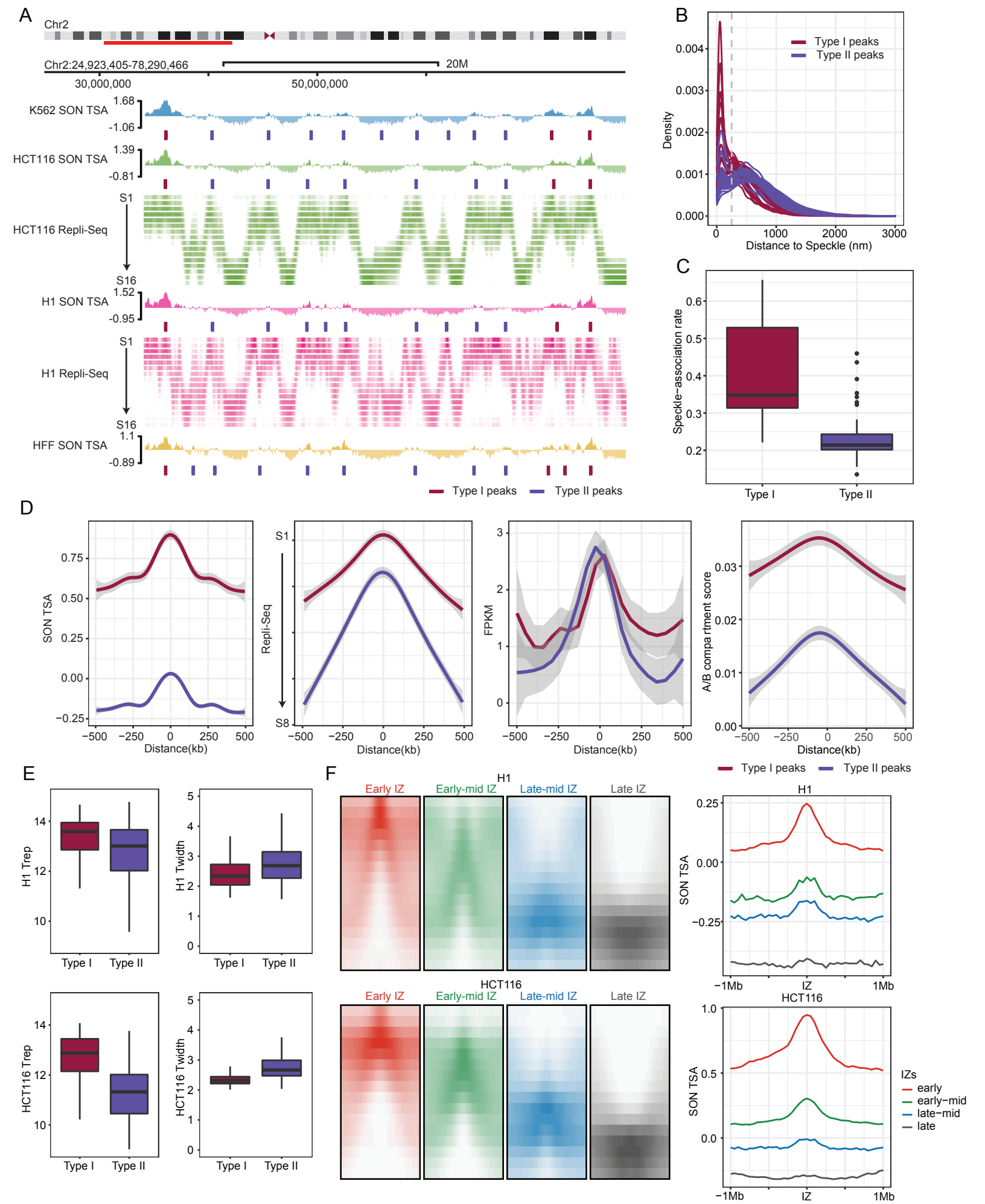
A
Chr2
Chr2:24,923,405-78,290,466
20M
30,000,000
50,000,000
K562 SON TSA
1.68
-1.06
HCT116 SON TSA
1.39
-0.81
HCT116 Repli-Seq
S1
S16
H1 SON TSA
1.52
-0.95
H1 Repli-Seq
S1
S16
HFF SON TSA
1.1
-0.89
Type I peaks
Type II peaks
B
Type I peaks
Type II peaks
Density
Distance to Speckle (nm)
C
Speckle−association rate
Type I
Type II
D
SON TSA
Distance(kb)
Repli-Seq
S1
S8
FPKM
A/B compartment score
Type I peaks
Type II peaks
E
H1 Trep
H1 Twidth
HCT116 Trep
HCT116 Twidth
Type I
Type II
F
H1
HCT116
Early IZ
Early-mid IZ
Late-mid IZ
Late IZ
SON TSA
−1Mb
IZ
1Mb
IZs
early
early−mid
late−mid
late

Figure 3

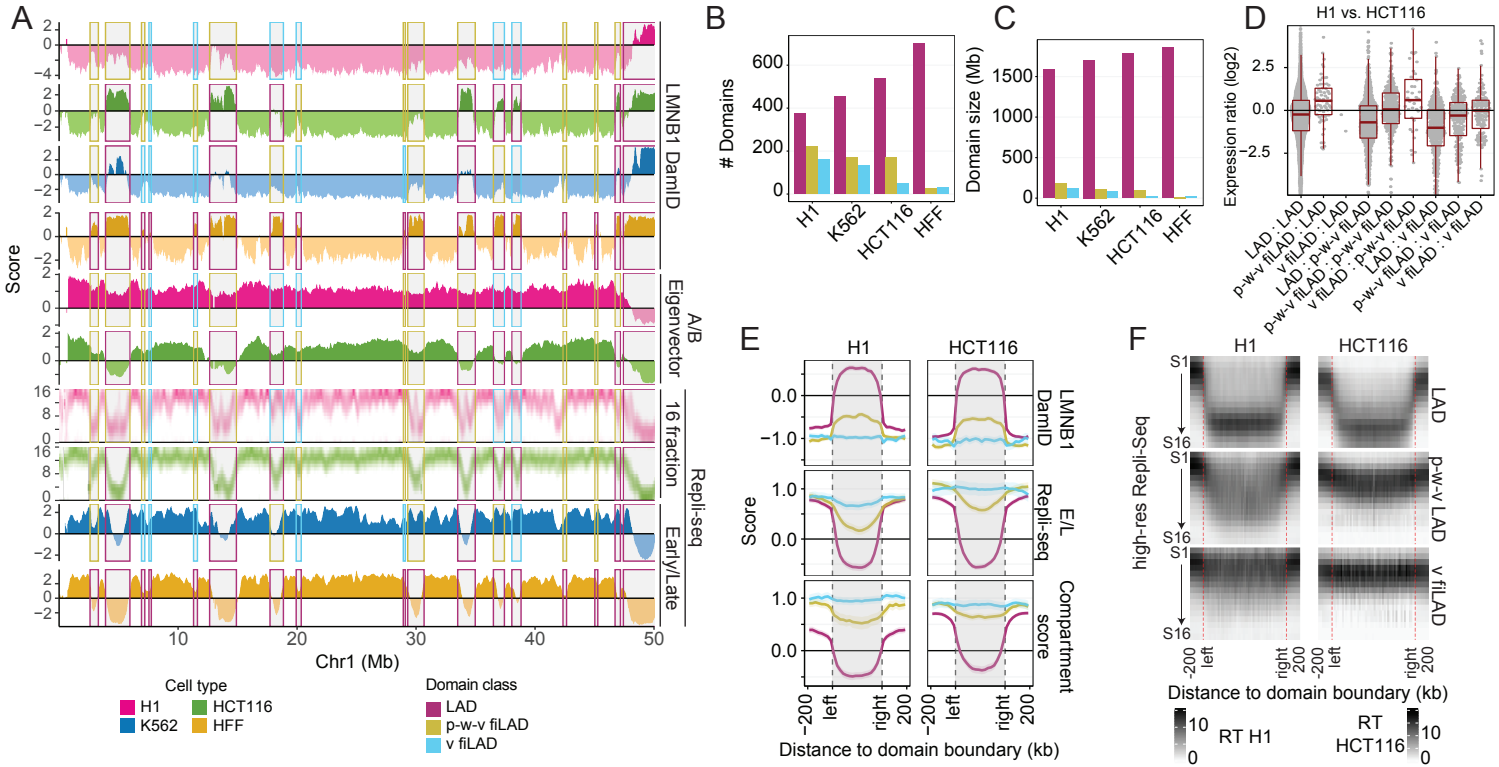
A
Score
LMNB1 DamID
A/B Eigenvector
16 fraction
Repli-seq
Early/Late
Chr1 (Mb)
Cell type
H1
HCT116
K562
HFF
Domain class
LAD
p-w-v fiLAD
v fiLAD
B
Domains
H1
K562
HCT116
HFF
C
Domain size (Mb)
D
H1 vs. HCT116
Expression ratio (log2)
LAD : LAD
p-w-v fiLAD : LAD
v fiLAD : LAD
LAD : p-w-v fiLAD
p-w-v fiLAD : p-w-v fiLAD
v fiLAD : p-w-v fiLAD
LAD : v fiLAD
p-w-v fiLAD : v fiLAD
v fiLAD : v fiLAD
E
H1
HCT116
LMNB1 DamID
E/L Repli-seq
Compartment score
Score
Distance to domain boundary (kb)
left
right
F
high-res Repli-Seq
S1
S16
LAD
p-w-v LAD
v fiLAD
Distance to domain boundary (kb)
RT H1
RT HCT116

Figure 4

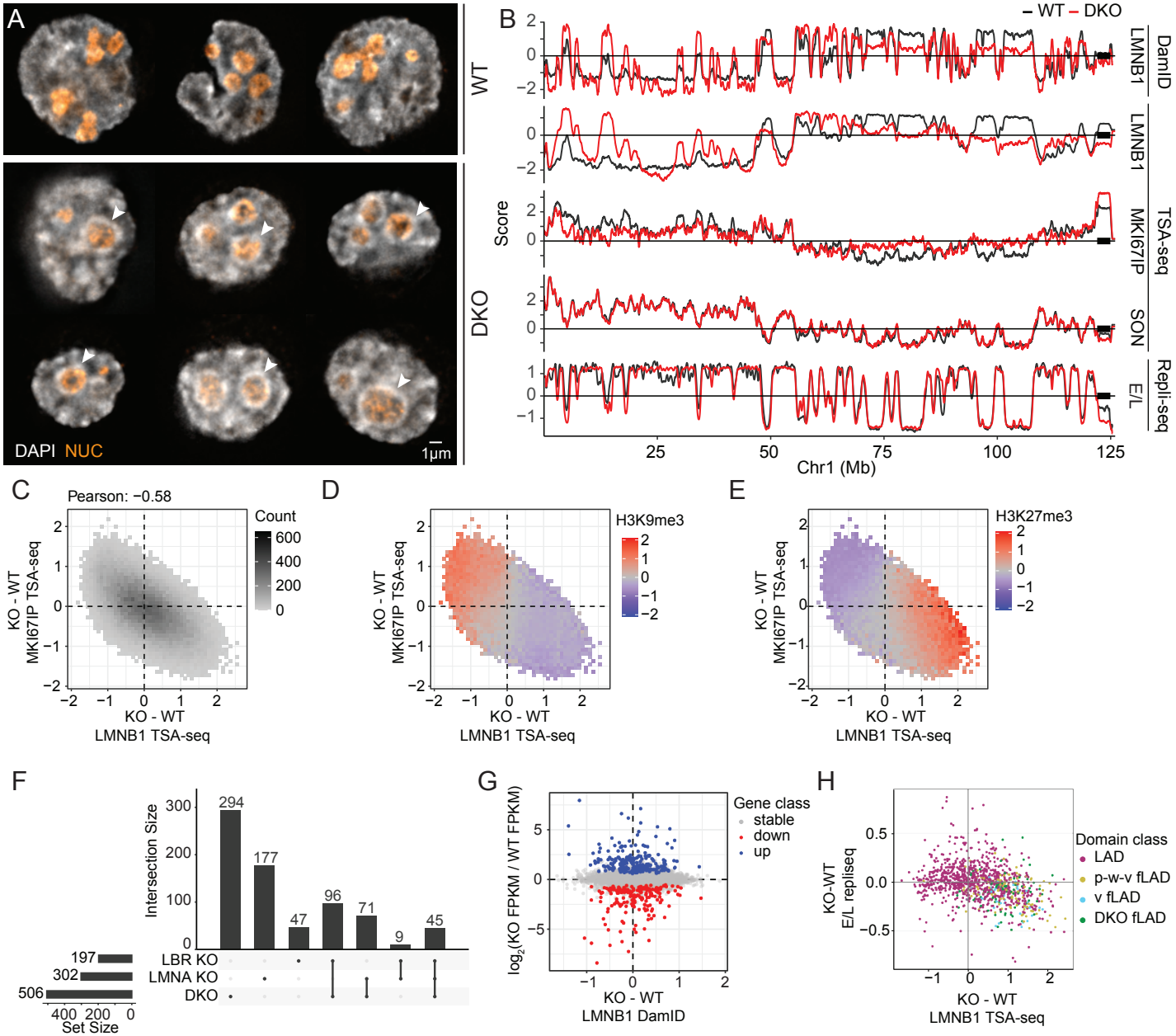
A
DAPI NUC
1µm
B
WT
DKO
WT DKO
Score
LMNB1
DamID
MKI67IP
TSA-seq
SON
E/L
Repli-seq
Chr1 (Mb)
C
Pearson: −0.58
Count
KO - WT
MKI67IP TSA-seq
LMNB1 TSA-seq
D
H3K9me3
E
H3K27me3
F
Intersection Size
Set Size
LBR KO
LMNA KO
DKO
294
177
47
96
71
9
45
197
302
506
G
Gene class
stable
down
up
log2(KO FPKM / WT FPKM)
LMNB1 DamID
H
Domain class
LAD
p-w-v fLAD
v fLAD
DKO fLAD
KO-WT
E/L repliseq

Figure 5

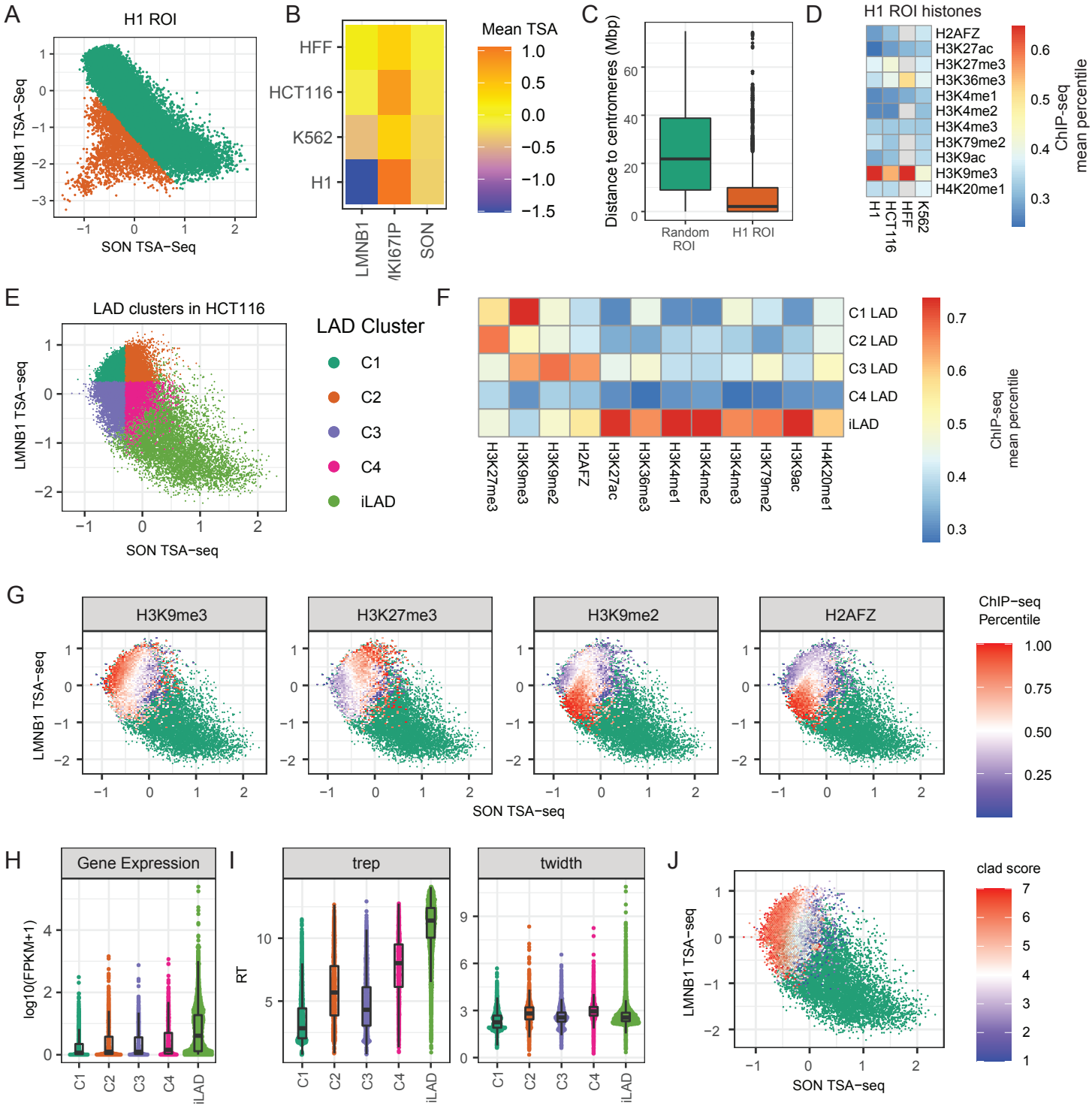
A
H1 ROI
LMNB1 TSA−Seq
SON TSA−Seq
B
HFF
HCT116
K562
H1
LMNB1
MKI67IP
SON
Mean TSA
1.0
0.5
0.0
−0.5
−1.0
−1.5
C
Distance to centromeres (Mbp)
Random ROI
H1 ROI
D
H1 ROI histones
H2AFZ
H3K27ac
H3K27me3
H3K36me3
H3K4me1
H3K4me2
H3K4me3
H3K79me2
H3K9ac
H3K9me3
H4K20me1
H1
HCT116
HFF
K562
ChIP-seq mean percentile
E
LAD clusters in HCT116
LMNB1 TSA−seq
SON TSA−seq
LAD Cluster
C1
C2
C3
C4
iLAD
F
C1 LAD
C2 LAD
C3 LAD
C4 LAD
iLAD
H3K27me3
H3K9me3
H3K9me2
H2AFZ
H3K27ac
H3K36me3
H3K4me1
H3K4me2
H3K4me3
H3K79me2
H3K9ac
H4K20me1
ChIP-seq mean percentile
G
H3K9me3
H3K27me3
H3K9me2
H2AFZ
LMNB1 TSA−seq
SON TSA−seq
ChIP−seq Percentile
H
Gene Expression
log10(FPKM+1)
C1
C2
C3
C4
iLAD
I
trep
twidth
RT
J
LMNB1 TSA−seq
SON TSA−seq
clad score

Figure 6

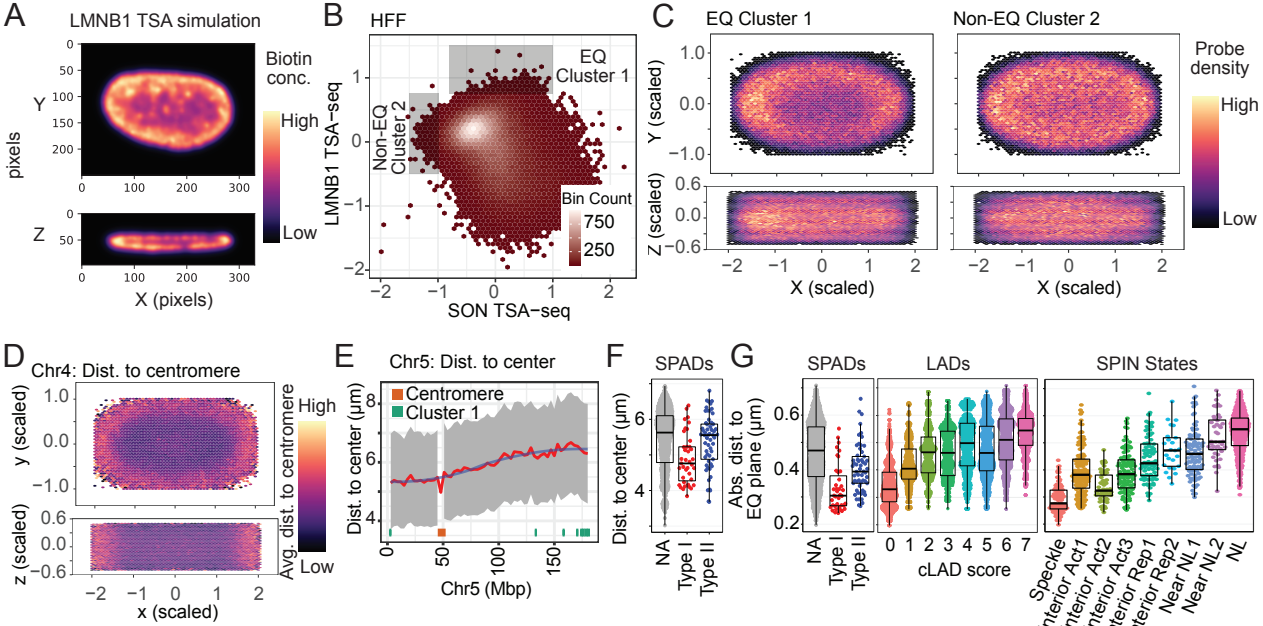
A
LMNB1 TSA simulation
Biotin conc.
High
Low
pixels
Y
Z
X (pixels)
B
HFF
EQ Cluster 1
Non-EQ Cluster 2
Bin Count
750
250
LMNB1 TSA−seq
SON TSA−seq
C
EQ Cluster 1
Non-EQ Cluster 2
Probe density
High
Low
Y (scaled)
Z (scaled)
X (scaled)
D
Chr4: Dist. to centromere
High
Low
Avg. dist. to centromere
y (scaled)
z (scaled)
x (scaled)
E
Chr5: Dist. to center
Centromere
Cluster 1
Dist. to center (μm)
Chr5 (Mbp)
F
SPADs
Dist. to center (μm)
NA
Type I
Type II
G
SPADs
LADs
SPIN States
Abs. dist. to EQ plane (μm)
NA
Type I
Type II
cLAD score
Speckle
Interior Act1
Interior Act2
Interior Act3
Interior Rep1
Interior Rep2
Near NL1
Near NL2
NL

Figure 7

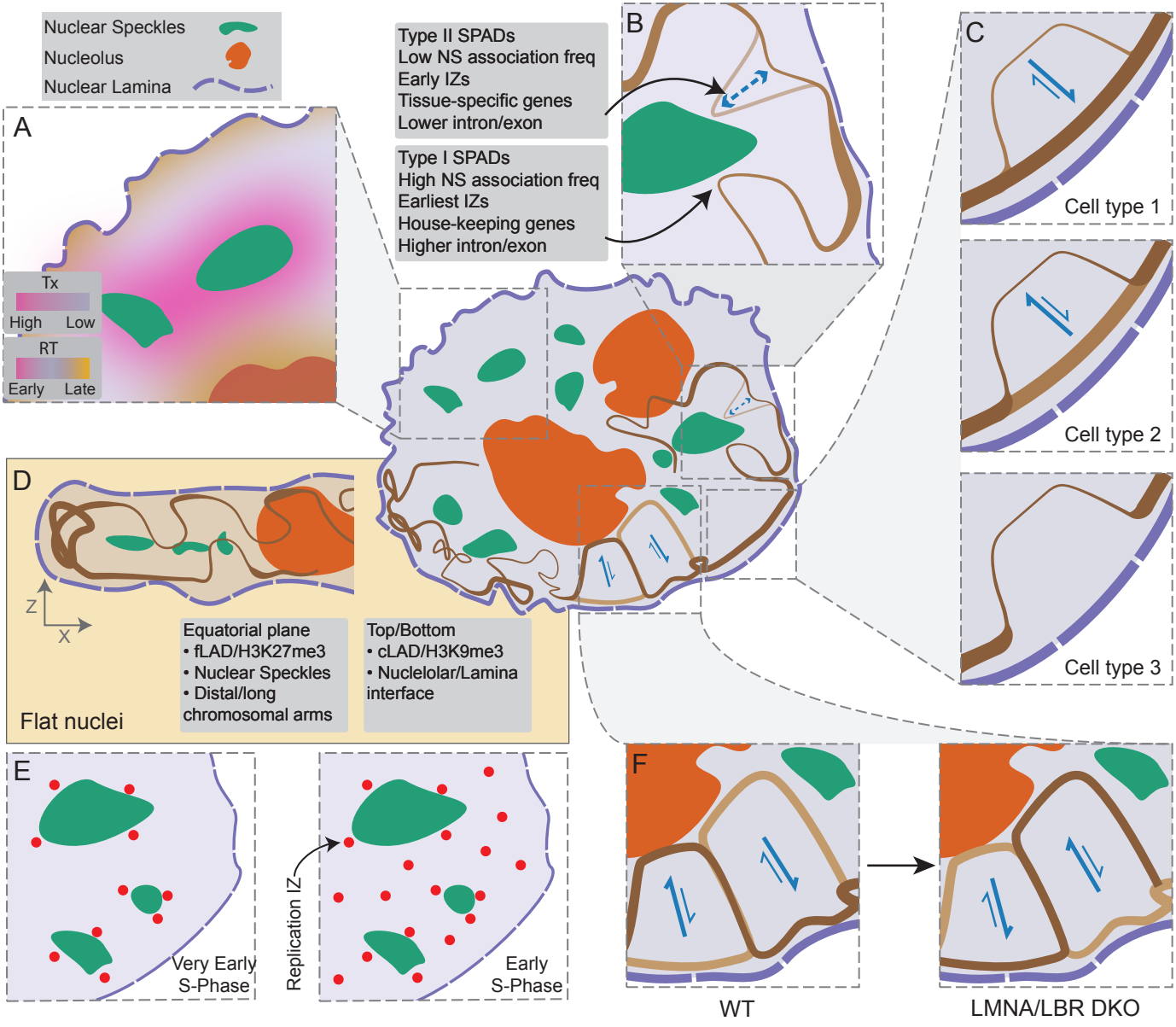
Nuclear Speckles
Nucleolus
Nuclear Lamina
A
Tx
High
Low
RT
Early
Late
Type II SPADs
Low NS association freq
Early IZs
Tissue-specific genes
Lower intron/exon
Type I SPADs
High NS association freq
Earliest IZs
House-keeping genes
Higher intron/exon
B
C
Cell type 1
Cell type 2
Cell type 3
D
Z
X
Equatorial plane
• fLAD/H3K27me3
• Nuclear Speckles
• Distal/long chromosomal arms
Top/Bottom
• cLAD/H3K9me3
• Nuclelolar/Lamina interface
Flat nuclei
E
Very Early S-Phase
Replication IZ
Early S-Phase
F
WT
LMNA/LBR DKO

Figure 8

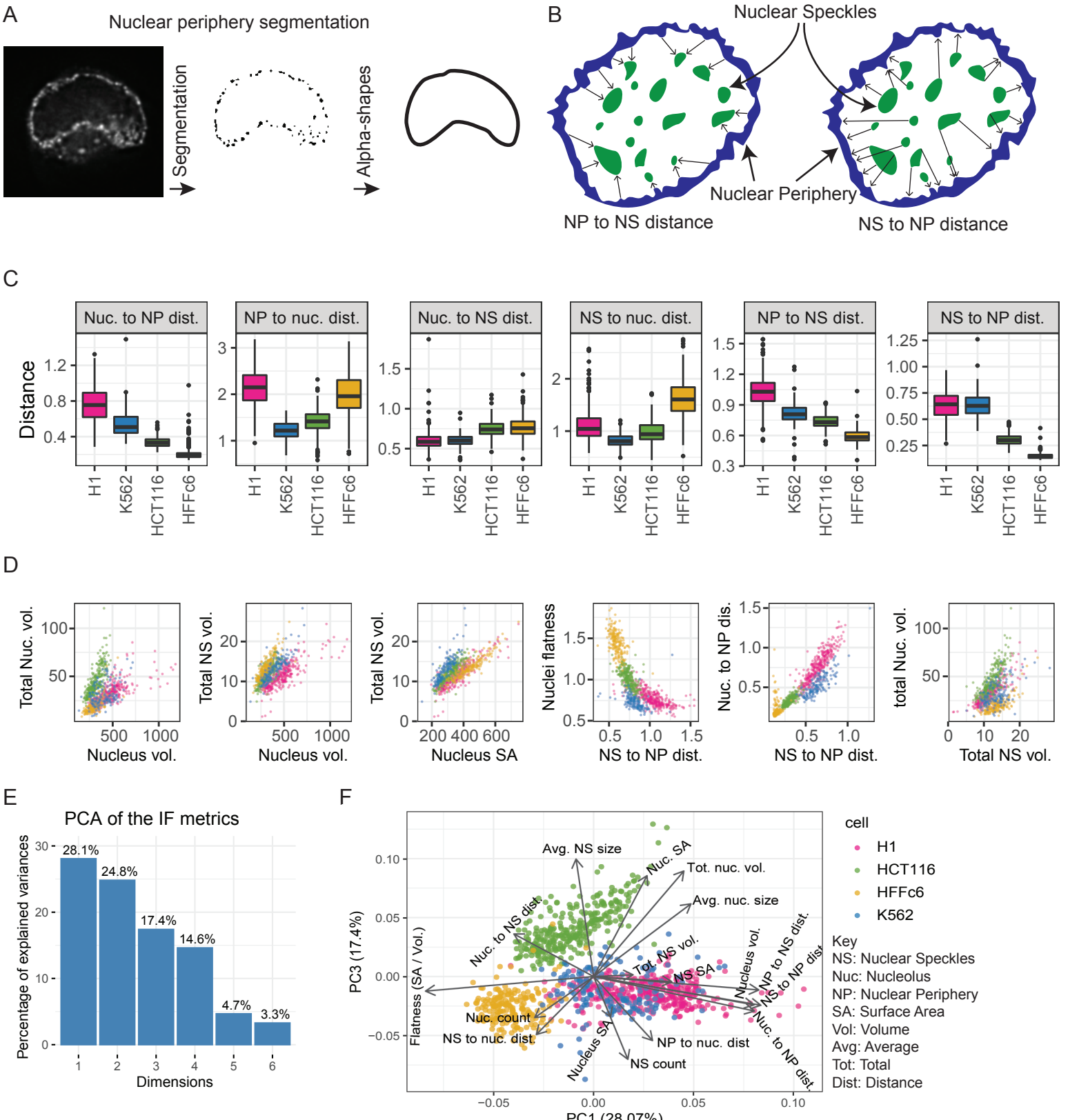

Supplementary Figure 1

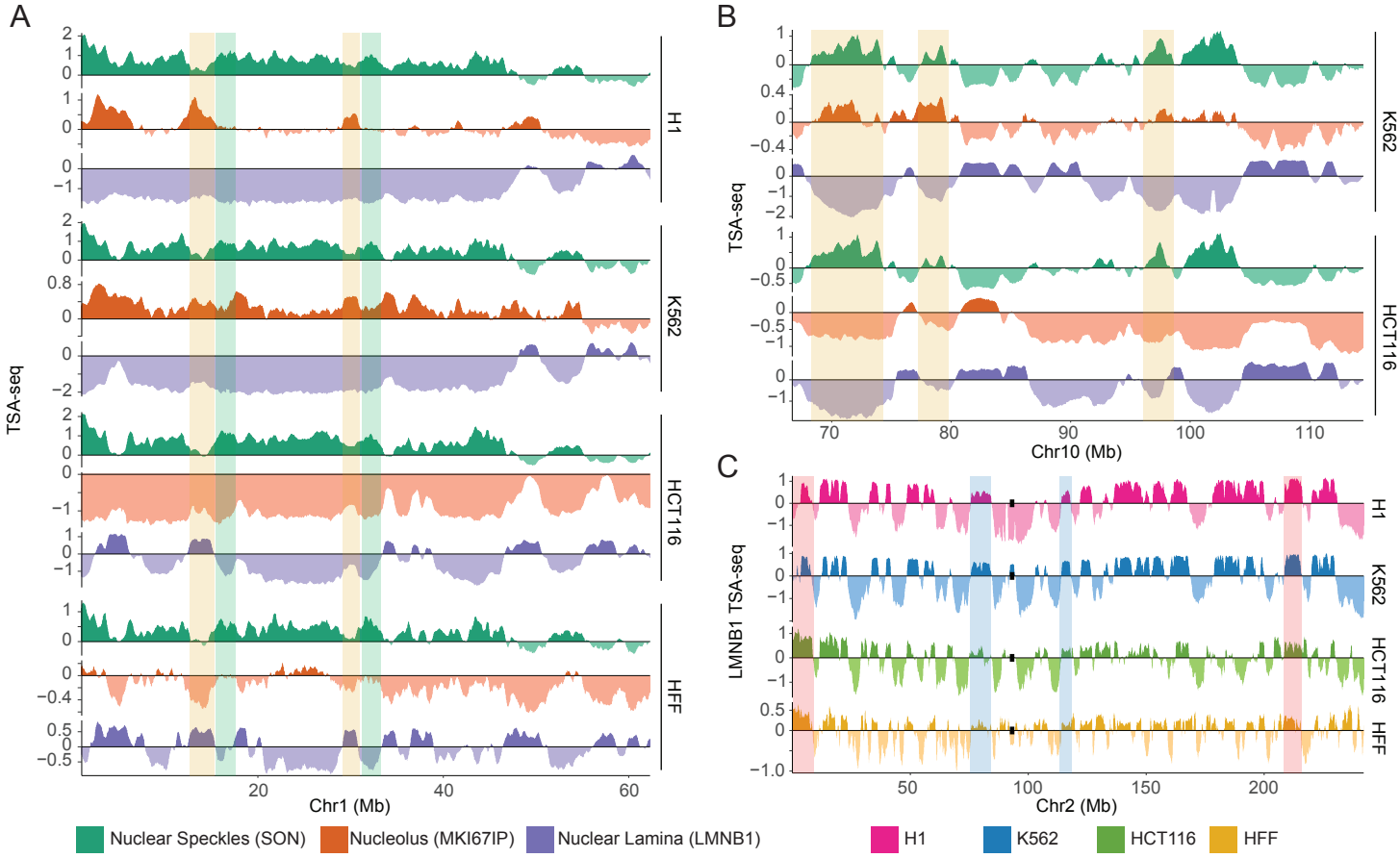

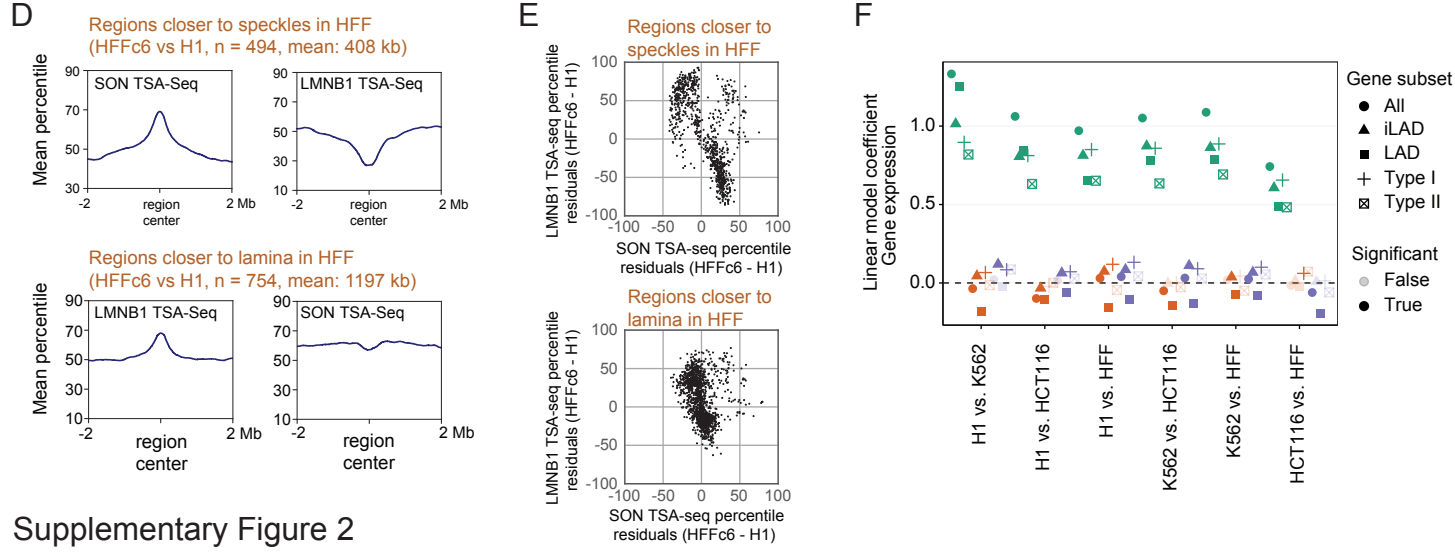

Supplementary Figure 2

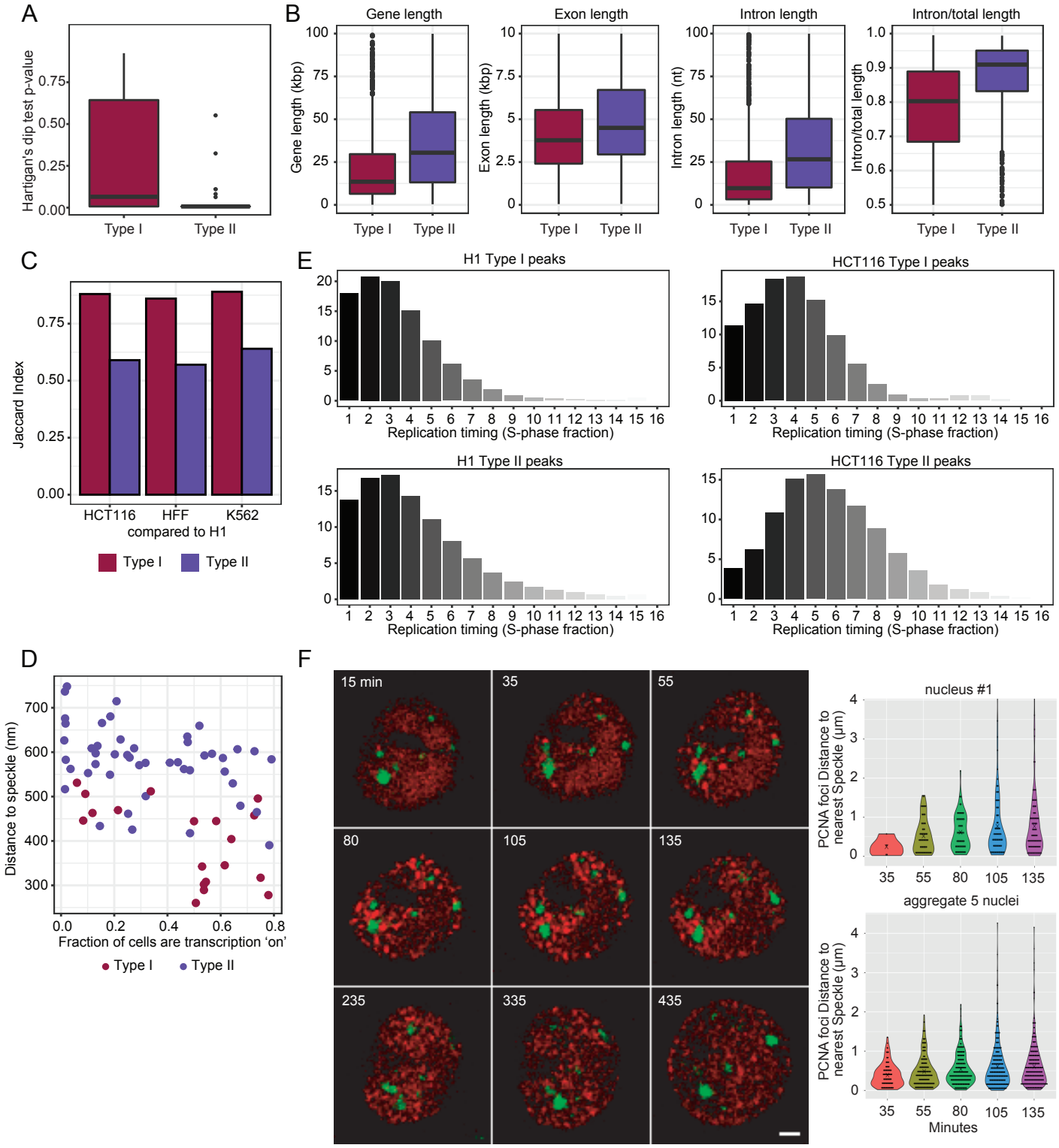

Supplementary Figure 3

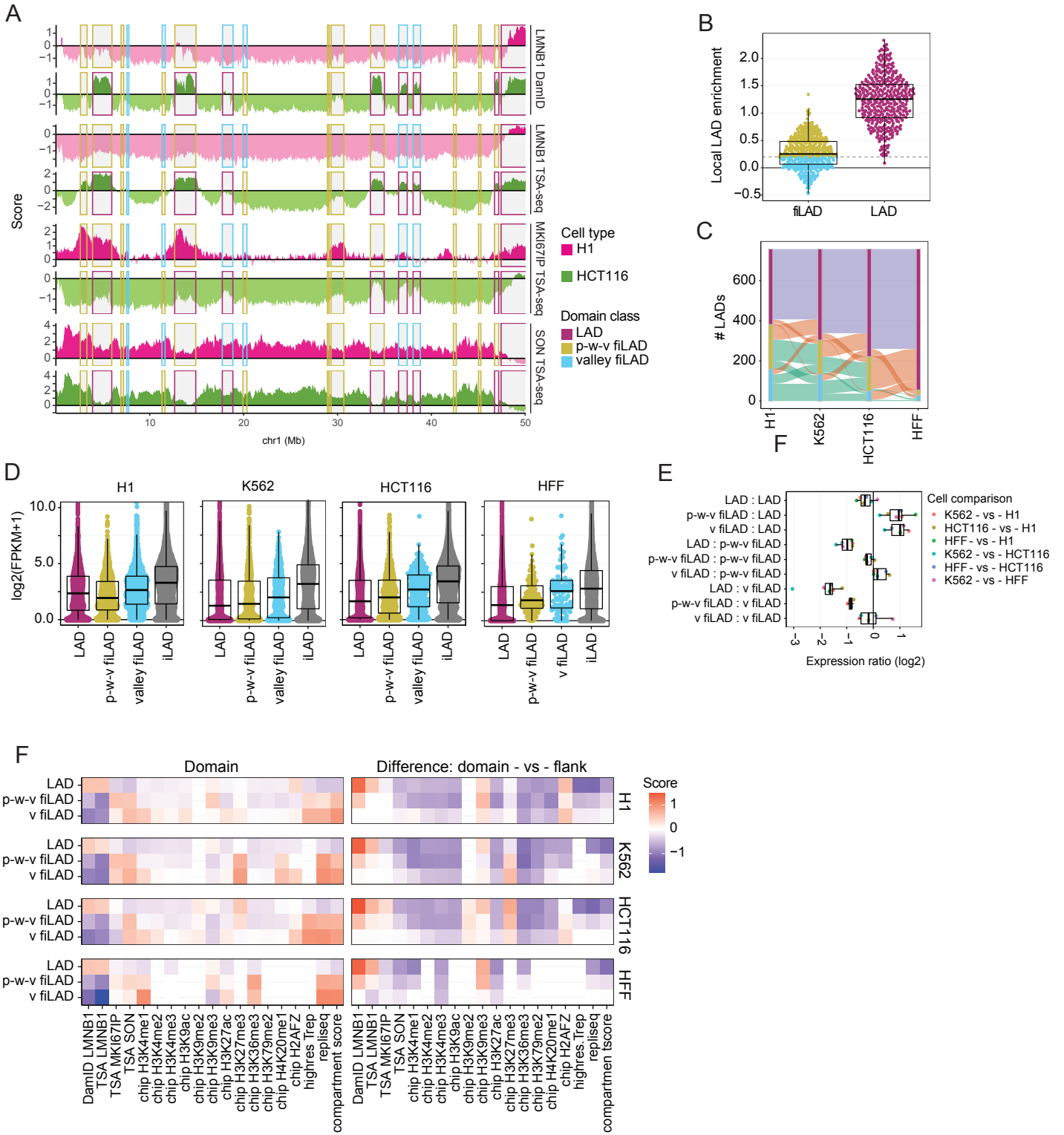

Supplementary Figure 4

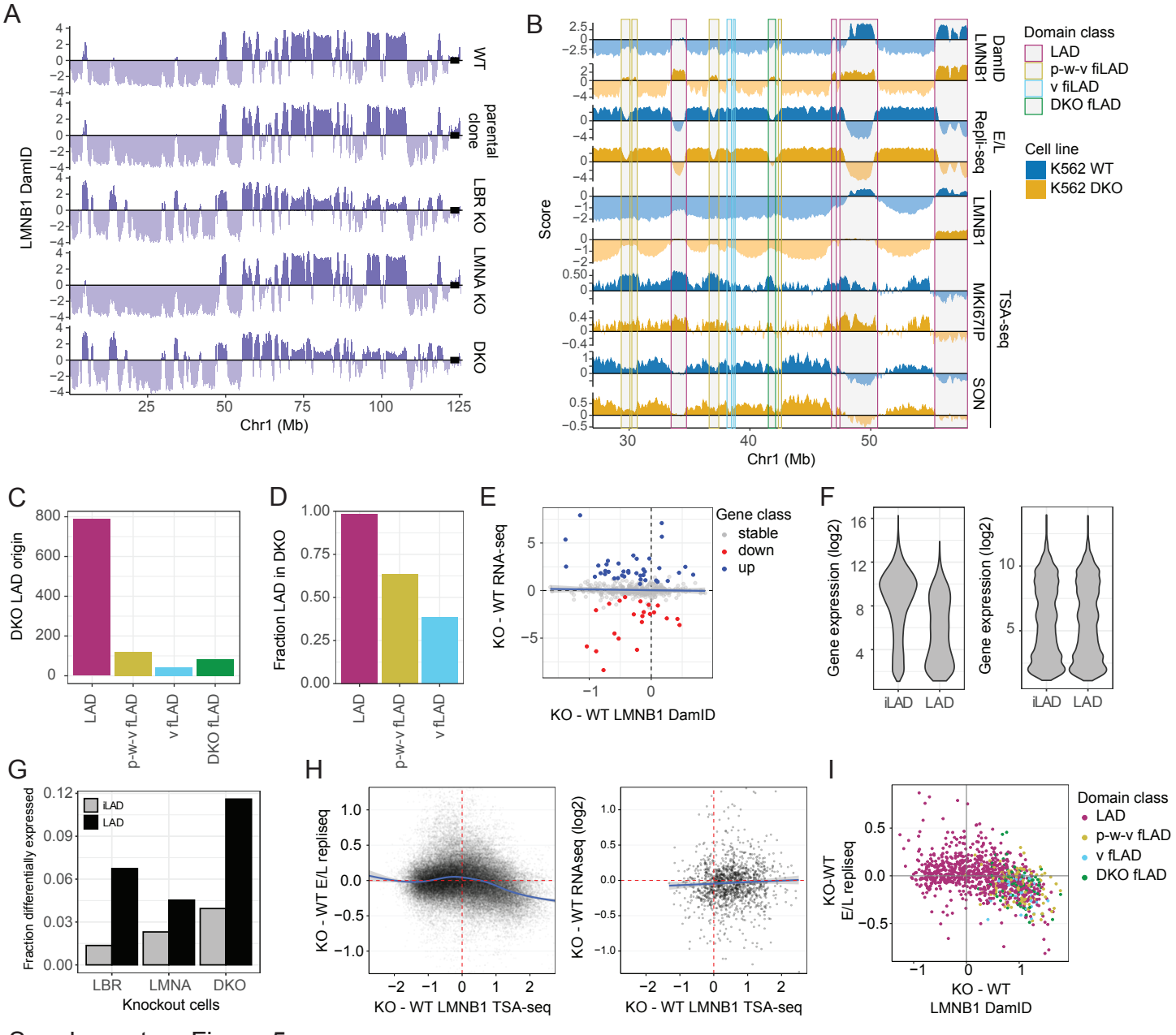

Supplementary Figure 5

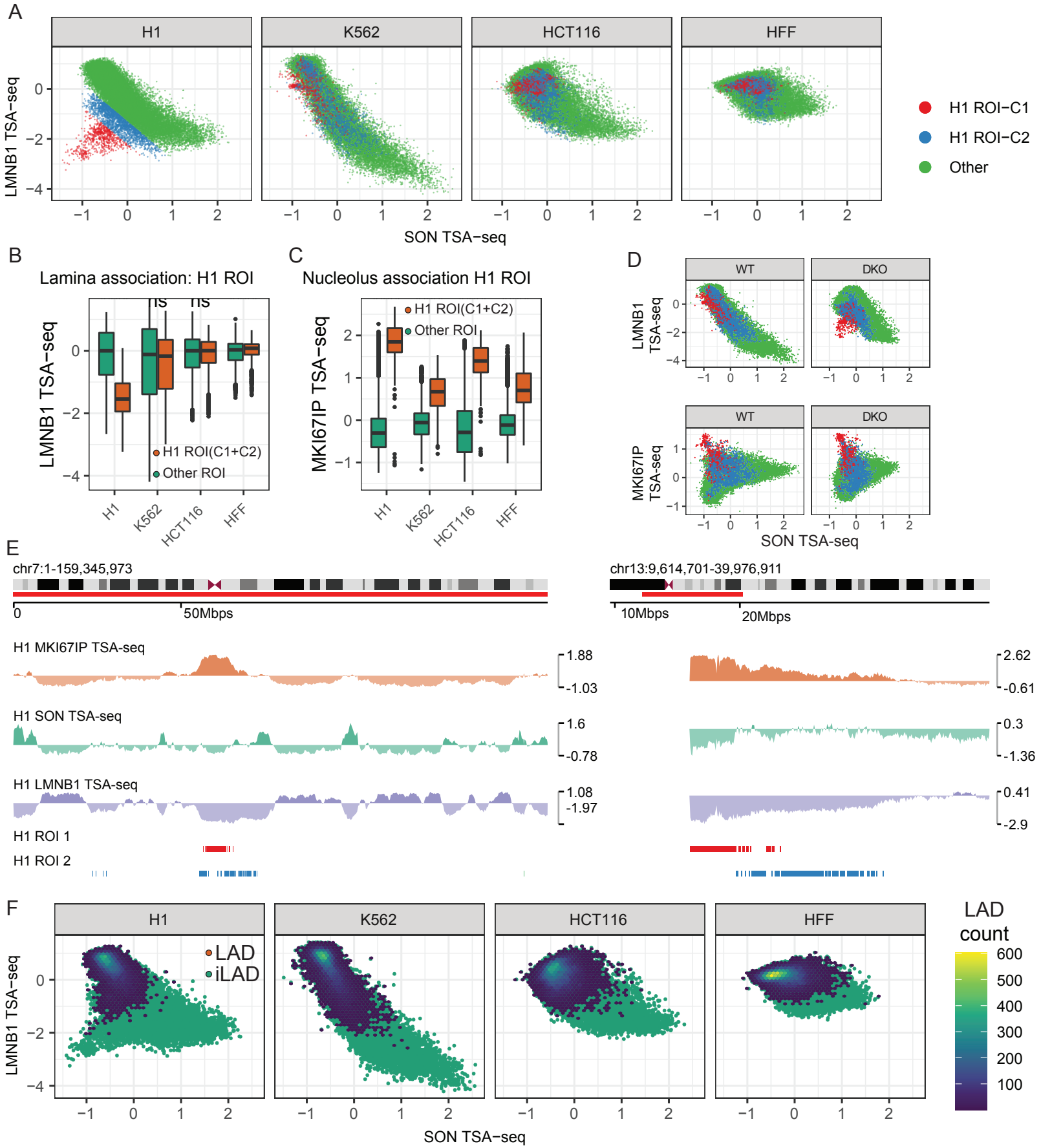

Supplementary Figure 6

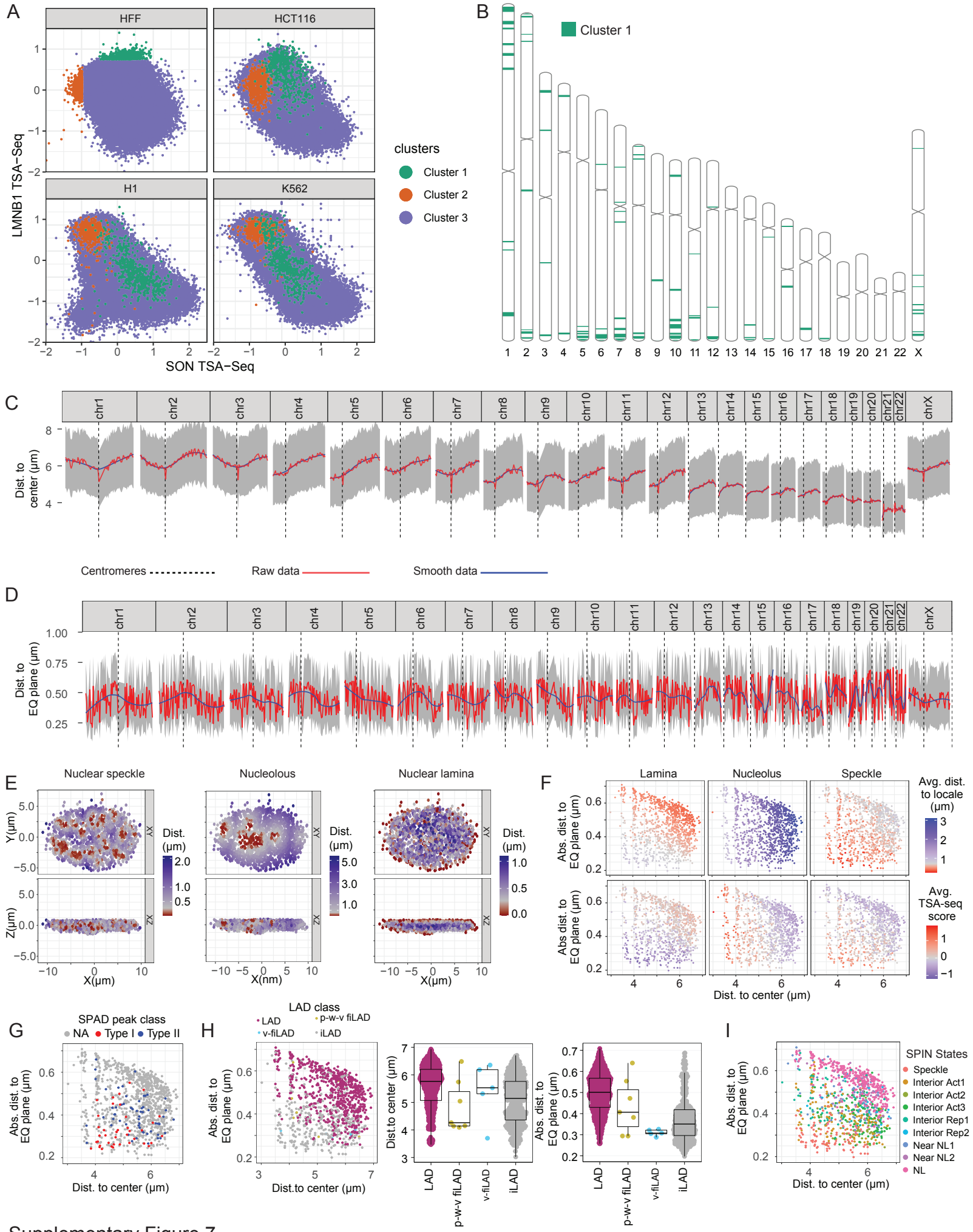

Supplementary Figure 7